Computational Geosciences (2020) 24:709–735
https://doi.org/10.1007/s10596-019-09834-7

ORIGINAL PAPER

Global/local model order reduction in coupled flow and linear thermal-poroelasticity

Horacio Florez[1] · **Eduardo Gildin**[1]

Received: 14 July 2018 / Accepted: 16 May 2019/ Published online: 10 June 2019

Abstract

Coupled flow and geomechanics computations are very complex and require solving large nonlinear systems. Such simulations are intense from both runtime and memory standpoint, which strongly hints at employing model order reduction (MOR) techniques to speed them up. Different types of Reduced-Order Models (ROM) have been proposed to alleviate this computational burden. MOR approaches rely on projection operators to decrease the dimensionality of the problem. We first execute a computationally expensive "offline" stage, during which we carefully study the full order model (FOM). Upon creating a ROM basis, we then perform the cheap "online" stage. Our reduction strategy estimates a ROM using proper orthogonal decomposition (POD). We determine a family of solutions to the problem, for a suitable sample of input conditions, where every single realization is so-called a "snapshot." We then ensemble all snapshots to determine a compressed subspace that spans the solution. Usually, POD employs a fixed reduced subspace of global basis vectors. The usage of a global basis is not convenient to tackle problems characterized by different physical regimes, parameter changes, or high-frequency features. Having many snapshots to capture all these variations is unfeasible, which suggests seeking adaptive approaches based on the closest regional basis. We thus develop such a strategy based on local POD basis to reduce one-way coupled flow and geomechanics computations. We partition the time window to adequately capture regimes such as depletion/build-up and decreasing the number of snapshots per basis. We focus on linear elasticity and consider factors such as the role of the heterogeneity. We also assess how to tackle different degrees of freedom, such as the displacements (intercalated and coupled), pressure, and temperature, with MOR. Preliminary 2- and 3-D results show significant compression ratios up to 99.9% for the mechanics part. We formally compare FOM and ROM and provide time data to demonstrate the speedup of the procedure. Examples focus on linear and nonlinear poroelasticity. We employ continuous Galerkin finite elements for all of the discretizations.

Keywords Model order reduction · Proper orthogonal decomposition · Elasticity · Continuous Galerkin

1 Introduction

Coupled flow and geomechanics simulations are highly complex and involve solving nonlinear algebraic systems of millions of equations and unknowns. Such simulations allow assessing the induced stresses changes that hydrocarbon production or the injection of fluids in a reservoir (RS) produce in the surrounding rock mass. These studies often include compaction and subsidence that pose harmful and costly effects such as in wells casing, cap-rock stability, faults reactivation, and environmental issues as well.

The simulation of the coupled flow and geomechanics is paramount to the design of hydraulic fracturing campaigns involving well/fracture placements in unconventional reservoirs. Although these simulations are challenging in their own right, e.g., selection of the coupling parameters and the proper choices in the collection of the real scenarios for the joint flow and geomechanics simulation, they have already become computationally intensive due to mesh resolution that is required to resolve the flow around the fractures. Furthermore, a substantial computational effort is needed if uncertainty quantification (UQ) has to be added to the process [23]. UQ relies on parametric studies that are intense from both CPU time and memory requirements. The CPU burden, thus, strongly suggests the use of some form of

✉ Horacio Florez
florezg@gmail.com; hflorez@tamu.edu

[1] Department of Petroleum Engineering, Texas A & M University, 3116 TAMU, College Station, TX 77843, USA

model approximations or reduced complexity frameworks, e.g., model order reduction (MOR) techniques, to perform simulations in real time that allow decision-making in a timely fashion.

We already recognized the increasing role of geomechanics in petroleum reservoir engineering as deeper formations are exploited, and also more complex processes are considered. For instance, the modeling of thermal fracturing and vapor injection, i.e., thermal oil recovery processes, require coupling flow, thermal and mechanical simulators. These applications encompass high pressures and temperatures, leading to substantial volume changes and induced stresses [49, 62]. For such problems, conventional reservoir modeling fails to provide an accurate analysis [45, 53], which is why we present herein a simple linear thermo-elastic model as the first step towards tackling these challenges in the future. One of the numerical examples comprises one-way coupling of nonlinear heat transfer and elasticity.

MOR has been applied extensively in reservoir simulation to mitigate the high computational cost of what we call a "single-physics" environment, e.g., multiphase flow in porous media [33, 35, 57, 58, 63] but, its application to coupled multiphysics, as in the case of combined flow and geomechanics, has been minimal. To the best of our knowledge, the first application of MOR in this scenario was introduced in [17, 24]. According to [35, 58], the most promising methods for model reduction of flow alone are the POD-DEIM and the TPWL and all of their variants. The central idea of these methods is the projection of the high dimensional residual and Jacobian into a much smaller subspace through a Galerkin projection. To this end, the proper orthogonal decomposition (POD) method is the core of these approximations. POD-like approaches usually consist of the following: a computationally expensive "offline" stage whereby the fine-scale (or full order model (FOM)) is adequately studied at carefully selected points in the input parameter space to compute a representative snapshot or the state-space. Then, a reduced subspace whose basis is used to obtain a ROM is calculated based on a singular value decomposition (SVD) of this snapshot matrix. Finally, during the inexpensive "online" stage, the ROM is solved, and its solutions expanded back onto the original space, see for instance [7, 20, 33].

MOR based on POD heavily depend on the set of collected snapshots obtained in the offline step of the algorithm. We compute a family of solutions spanning the uncertainty in the input space, where every single realization is a "snapshot." We then ensemble all snapshots as column vectors, to compute a compressed subspace via POD, which spans the FOM solution (see, for instance, [7, 9]). An important issue is that the projection basis, and hence the ROM, only contains information that is present in the ensemble of snapshots. Thus, a careful snapshot selection is critical to constructing a successful POD basis (e.g., [60]). The standard POD implementation implies approximating the problem of interest in a fixed reduced subspace of global basis vectors. However, this is not convenient to tackle models characterized by different physical regimes, parameter variations, or moving features such as discontinuities and fronts. Having a large number of snapshots to capture all these regimes/local features makes global POD impractical according to [2, 20]. This drawback suggests seeking for adaptive approaches based on a regional basis and alternatives to POD.

The localized POD has been used in the case of flow simulation in [32]. In this case, K-means was used to cluster the temporal snapshots due to a change in the flow regime. Kerfriden et al. [37] described a bridge between POD-based MOR techniques and the classical Newton/Krylov solvers. Their method overcomes some of the POD's drawbacks found on structural problems involving plasticity or damage: find an initial snapshot that is adequate to represent the solution of the damaged structure accurately as well as significant topological changes that may occur in it. They proposed a corrective tool for the adaptive MOR for such mechanical problems whose novelty lies in the fact that integrates corrections inside the POD projection framework. Hernández et al. [36] presented a novel model order reduction technique for the solution of the fine-scale equilibrium problem arising in computational homogenization. Their method relies on a reduced set of empirical shape functions computed via POD. They also chose interpolation points based on not only accuracy but also by on stability considerations. The resulting speedup factor is over $3\times$. Similarly, Corigliano et al. [11] combined using domain decomposition and snapshot-based POD techniques for elastic-plastic applications in structural dynamics. They attained a $2\times$ speedup. Kerfriden et al. [38] propose a local/global MOR method to circumvents the difficulties of simulating highly nonlinear mechanical failures. Niroomandi et al. [51, 52] extended the proper generalized decomposition methods to nonlinear hyperelasticity problems, which results in an approximation of the solution in the form of a series expansion. The technique renders accurate results that can be stored in a compact form for tackling real-time applications.

This paper introduces a MOR algorithm that, as we will demonstrate, provides a substantial speedup, up to 50X if we combine with multi-threading post-processing, for one- and two-way coupled problems involving thermo-poroelasticity. We also propose a local-in-time POD scheme, i.e., POD with time partitioning to tackle geomechanics problems with distinct and thus incompatible transient regimes such as those arising from non-monotonic sequential production and injection scenarios. We employ a continuous Galerkin finite element formulation for linear isotropic elasticity

and slightly compressible single-phase flow. We consider nonlinear transient heat transfer as well. We include concrete numerical examples covering two- and three-dimensional problems of practical interest. The sample problems employ triangular, quadrilateral, and hexahedral meshes and include standard boundary conditions (BCS).

We organize the remainder of the paper as follows. The first section presents the mathematical models of the governing partial differential equations. The second revises the proposed MOR method and also shortly discusses POD properties and introduces LPOD. In the third one, we present concrete numerical examples of our MOR algorithm. The last sections state concluding remarks and future work.

2 Mathematical model for thermo-poroelasticity

We discuss the governing equations for linear homogeneous isotropic thermo-poroelasticity and their finite element (FE) formulation. We skip many of the details for the sake of brevity, and a complete treatment can be found in [13, 16, 27, 43]. We consider a bounded domain $\Omega \subset \mathbb{R}^n, n = 2, 3$ and its boundary is $\Gamma = \partial\Omega$, and a time interval of interest $]0, \Im[$. Let $\mathcal{T}_h$ be a non-degenerate, quasi-uniform conforming partition of Ω composed of convex elements. As shown by [4, 31], the continuity equation and Darcy's law yield:

$$\frac{\partial \phi^*}{\partial t} + \nabla \cdot \left(-\frac{1}{\mu} \underline{\underline{K}} \left(\nabla p - \rho g \nabla z \right) \right) = q \ , \tag{1}$$

where the parameters are ϕ^*, a model specific porosity, $\underline{\underline{K}}$ represents the absolute permeability tensor. The dynamic viscosity is μ, while ρ is the fluid density, as well as g, is the gravity acceleration constant, p is the fluid pressure, and q represents sources and sinks. Finally, the algorithmic porosity ϕ^* is defined by:

$$\phi^* = \phi^0 + \alpha \cdot \left(\nabla \cdot \underline{u} - \varepsilon_v^0 \right) + \frac{1}{M} \left(p - p^0 \right) \ , \tag{2}$$

where the additional parameters are accordingly α which is the Biot's constant, $\underline{u}$ represents the displacement vector, while ε_v^0 is the initial volumetric strain. Herein, M is the Biot's modulus, while ϕ^0 and p^0 define for a reference or initial state (see [12]). The common boundary conditions (BCS) for the pressure equation imply Neumann or no-flow namely:

$$\nabla p \cdot \hat{\underline{n}} = 0 \ \text{on} \Gamma, \tag{3}$$

and one should also consider an initial or reference pressure distribution in the whole domain. Herein $\hat{\underline{n}}$ is the outer unitary normal vector as usual. For the mechanics part, one begins from the equilibrium equation for a quasi-steady process:

$$\begin{aligned} -\nabla \cdot \underline{\underline{\sigma}} &= \underline{f} \ \text{in} \Omega \ ; \Gamma = \Gamma_D^u \cup \Gamma_N^u \\ \underline{u} &= \underline{0} \ \text{on} \Gamma_D^u \\ \underline{t} &= \underline{\underline{\sigma}} \cdot \hat{\underline{n}} \ \text{on} \Gamma_N^u \end{aligned} \tag{4}$$

where $\underline{\underline{\sigma}}$ is the stress tensor, $\underline{f}$ corresponds to the vector of body forces, such as gravity, for instance. One can decompose BCS in Dirichlet type, i.e., Γ_D^u, and Neumann type BCS, i.e., Γ_N^u, where the external tractions are known or prescribed. Hooke's law combined with Biot's poroelastic theory defines $\underline{\underline{\sigma}}$ by the following expression:

$$\underline{\underline{\sigma}} = \underline{\underline{C}} : \underline{\underline{\varepsilon}} - \left[\alpha \left(p - p^0 \right) + 3K\beta \left(T - T^0 \right) \right] \underline{\underline{\delta}} \ ; \underline{\underline{C}} = \lambda \underline{\underline{\delta}} \otimes \underline{\underline{\delta}} + 2G \underline{\underline{I}} \ , \tag{5}$$

where the operator ":" represents the tensor or dyadic product, $T = T(x, t)$ is the temperature, $\underline{\underline{C}}$ is the elastic moduli, β corresponds to the coefficient of thermal dilatation while K is the bulk modulus. The Kronecker delta becomes $\underline{\underline{\delta}}$ while λ, and G, are the Lamé constants, and $\underline{\underline{I}}$ represents the fourth-order identity tensor. The strain tensor $\underline{\underline{\varepsilon}}$ is given by:

$$\underline{\underline{\varepsilon}} = \nabla^s \underline{u} = \frac{1}{2} \left[\nabla \underline{u} + \left(\nabla \underline{u} \right)^T \right] \ . \tag{6}$$

We derive a weak form by substituting Eq. (2) into Eq. (1) and then multiply by a test function $v \in H_0^1(\Omega)$ and integrating over Ω and using the Gauss-divergence theorem, which yields:

$$\begin{aligned} &\int_\Omega \left(\tfrac{1}{M} \tfrac{\partial p}{\partial t} v + \alpha v \nabla \cdot \dot{\underline{u}} + \tfrac{1}{\mu} \underline{\underline{K}} \cdot \nabla p (\nabla v)^T \right) \cdot dx = \int_\Omega q \cdot v dx + \\ &\int_\Omega \left(\tfrac{\rho g}{\mu} \underline{\underline{K}} \cdot \nabla z (\nabla v)^T \right) dx + \int_{\partial \Omega_N^p} v \tfrac{1}{\mu} \underline{\underline{K}} (\nabla p - \rho g \nabla z) \cdot \hat{\underline{n}}^T ds \ . \end{aligned} \tag{7}$$

We proceed analogously with the equilibrium Eq. (4), by testing against a given virtual displacement, $\underline{\chi}$. We arrive at:

$$\int_\Omega \left(\nabla \underline{\chi} \right)^T : \underline{\underline{\sigma}} d\Omega = \int_{\partial \Omega_N^u} \underline{\chi}^T \cdot \underline{t} ds + \int_\Omega \underline{\chi}^T \cdot \underline{f} d\Omega \tag{8}$$

where $\underline{t} = \underline{\underline{\sigma}} \cdot \hat{\underline{n}}$ are the tractions applied as Neumann BCS. Equation (8) is the virtual work statement. We can take the FE space as a finite-dimensional subspace of the continuous Sobolev spaces [54]:

$$\mathcal{C}_k \left(\mathcal{T}_h \right) = \left\{ v \in L^2 \left(\Omega \right) \ : \forall e \in \mathcal{T}_h, \ v|_e \in \mathbb{P}_k \left(e \right) \right\} \tag{9}$$

where $\mathbb{P}_k(e)$ represents the space of polynomials of total degree less than or equal to k, $\mathcal{C}_k(\mathcal{T}_h)$ is called test functions that are continuous along the given element's edges. We often represent the primary variables in the element e, i.e. displacements and pressure, as nodal values multiplied by shape or interpolation functions [6]:

$$p_e^h \left(\underline{x} \right) = \left(\underline{\Pi}^e \right)^T \cdot \underline{p}^e \ ; \underline{u}_e^h \left(\underline{x} \right) = \underline{\underline{\Psi}}^e \cdot \underline{u}^e \tag{10}$$

where $\underline{\Pi}^e$ and $\underline{\underline{\Psi}}^e$ are matrices of shape functions given by:

$$\begin{aligned} {\Pi_i}^e &= {\psi_i}^e\left(\underline{x}\right) \\ {\Psi_{ij}}^e &= \begin{cases} {\psi_k}^e\left(\underline{x}\right) \text{ if} j = \underline{\mathrm{j}} \\ 0 \text{ otherwise} \end{cases} \\ \underline{\mathrm{j}} &= \mathrm{nDOF}\cdot(k-1)+i \;;k = 1\ldots nn \end{aligned} \tag{11}$$

here nn is the number of nodes in the given element, $i = 1\ldots nn$, $j = 1\ldots nn\cdot n$ and nDOF is the number of degrees of freedom which equals the space dimension. Now the engineering strain $\underline{\hat{\varepsilon}}$ is defined by:

$$\underline{\hat{\varepsilon}} = \underline{\underline{B}}\cdot\underline{u}^e \;;\underline{\underline{B}} = \underline{\underline{D}}\cdot\underline{\underline{\Psi}}^e \tag{12}$$

where $\underline{\underline{D}}_{(n)}$ is defined as:

$$\underline{\underline{D}}^T_{(2)} = \begin{bmatrix} \partial_x & 0 & \partial_y \\ 0 & \partial_y & \partial_x \end{bmatrix} ;\underline{\underline{D}}^T_{(3)} = \begin{bmatrix} \partial_x & 0 & 0 & \partial_y & \partial_z & 0 \\ 0 & \partial_y & 0 & \partial_x & 0 & \partial_z \\ 0 & 0 & \partial_z & 0 & \partial_x & \partial_y \end{bmatrix}. \tag{13}$$

Finally, substituting the generalized Hooke's law Eq. (5) into Eq. (8) and using Eq. (7) lead to the FE model for linear isotropic poroelasticity, thus:

$$\begin{bmatrix} 0 & 0 \\ \underline{\underline{\mathrm{Q}}}^T & \underline{\underline{\mathrm{S}}} \end{bmatrix}\frac{d}{dt}\begin{Bmatrix} \underline{u} \\ \underline{p} \end{Bmatrix} + \begin{bmatrix} \underline{\underline{\mathrm{K}}} & -\underline{\underline{\mathrm{Q}}} \\ 0 & \underline{\underline{\mathrm{H}}} \end{bmatrix}\begin{Bmatrix} \underline{u} \\ \underline{p} \end{Bmatrix} = \begin{Bmatrix} \underline{f_u} \\ \underline{f_p} \end{Bmatrix}. \tag{14}$$

where the matrixes are given by:

$$\begin{aligned} \underline{\underline{\mathrm{S}}} &= \int_\Omega \tfrac{1}{M}\underline{\Pi}\cdot\underline{\Pi}^T dx \;;\underline{\underline{\mathrm{Q}}} = \int_\Omega \underline{\underline{B}}^T\alpha\underline{\omega}_{(n)}\cdot\underline{\Pi}dx \\ \underline{\underline{\mathrm{K}}} &= \int_\Omega \underline{\underline{B}}^T\underline{\underline{C}}\underline{\underline{B}}dx \;;\underline{f_u} = \int_{\partial\Omega^u_N}\underline{t}\cdot\underline{\underline{\Psi}}^T ds + \int_\Omega \underline{\underline{\Psi}}^T\underline{f}\cdot dx \\ \underline{\underline{\mathrm{H}}} &= \int_\Omega \tfrac{1}{\mu}\underline{\underline{K}}\nabla\underline{\Pi}\cdot\left(\nabla\underline{\Pi}\right)^T dx \;;\underline{\omega}_{(2)} = (1,1,0)^T \;;\underline{\omega}_{(3)} = (1,1,1,0,0,0)^T \\ \underline{f_p} &= \int_{\partial\Omega^p_N}\left(\tfrac{1}{\mu}\underline{\underline{K}}\nabla p\cdot\underline{n}\right)\cdot\underline{\Pi}ds + \int_\Omega \underline{\Pi}^T q\cdot dx + \int_\Omega\left(\tfrac{\rho g}{\mu}\underline{\underline{K}}\cdot\nabla\underline{\Pi}(\nabla z)^T\right)dx\,. \end{aligned} \tag{15}$$

We can obtain the loose coupling approach in different ways. Equation (16) shows one possible choice, where one solves the displacements first by taking the pressures from the previous timestep. Next, one updates the pressures by using the newest displacements:

$$\begin{aligned} \underline{\underline{\mathrm{K}}}\cdot\underline{u}^{(k+1)} &= f_u + \underline{\underline{\mathrm{Q}}}\left(\underline{p}^{(k)} - \underline{p}^{(0)}\right) \\ \underline{\underline{\mathrm{S}}}'\cdot\underline{p}^{(k+1)} &= \underline{\underline{\mathrm{S}}}''\cdot\underline{p}^{(k)} + \underline{f_p}\cdot\Delta t - \underline{\underline{\mathrm{Q}}}^T\left(\underline{u}^{(k+1)} - \underline{u}^{(k)}\right) \\ \underline{\underline{\mathrm{S}}}' &= \underline{\underline{\mathrm{S}}} + \theta\cdot\Delta t\cdot\underline{\underline{\mathrm{H}}} \\ \underline{\underline{\mathrm{S}}}'' &= \underline{\underline{\mathrm{S}}} - (1-\theta)\cdot\Delta t\cdot\underline{\underline{\mathrm{H}}}\,, \end{aligned} \tag{16}$$

where θ is the implicitness factor that lies between 0 and 1, while Δt represents the timestep size. One can define an iterative coupling scheme in different ways, but they all derive from the loose coupling approach by incorporating an internal iteration to update lagged quantities. For further details, please refer to [13, 41, 63]. Also notice that for thermal stresses, one can derive an equivalent pressure drop, after Eq. (5), i.e., $\Delta p(T) \equiv 3K\beta\left(T - T^0\right)/\alpha$, that renders Eq. (16) unchanged as shown by [18]. The next subsection presents discretizing the nonlinear energy equation to solve for the temperature field.

2.1 Nonlinear heat transfer equation

The transient nonlinear heat conduction in a given domain is as follows [17, 18, 61]:

$$\begin{aligned} \rho C_p\tfrac{\partial T}{\partial t} &= \nabla\cdot(\kappa\nabla T) + Q_T \;\mathrm{on}\Omega\times\,]0,\Im[\,, \\ T &= g\;\mathrm{on}\Gamma^T_D\times\,]0,\Im[\,, \\ n\cdot(\kappa\nabla T) &= h\;\mathrm{on}\Gamma^T_N\times\,]0,\Im[\,, \\ T(x,0) &= T_0(x)\,\forall x\in\Omega. \end{aligned} \tag{17}$$

Above, C_p is the heat capacity to constant pressure and $\kappa = \kappa(T)$ is the thermal conductivity. Q_T represents heat sources. Neumann BCS imply heat transfer via Fourier's law: adiabatic or no-flux BCS; $h = 0$ of most domain boundaries. We derive an FE formulation for model problem (17) by multiplying by a test function and integrate by parts and applying the Gauss-divergence theorem to arrive at the following bilinear form:

$$m(T,v) + k(T,v) - q(Q_T,v) - f(h,v) = 0\,, \tag{18}$$

where the functions are:

$$\begin{aligned} m(T,v) &= \int_{\Omega^e} v\rho C_p\partial_t T\cdot dx\,, \\ k(T,v) &= \int_{\Omega^e}\kappa\left(\nabla T\right)^T\cdot\nabla v\cdot dx\,, \\ q(Q_T,v) &= \int_{\Omega^e} v\cdot Q_T\cdot dx \;;f(h,v) = \int_{\Gamma^e_h} v\cdot h\cdot ds\,. \end{aligned} \tag{19}$$

Time discretization renders the local residual for the element e:

$$\underline{\mathcal{R}}_e^{(T_h)} \equiv \underline{\underline{M}} \cdot \left(\underline{T}^{(\ell)} - \underline{T}^{(m)}\right) + \Delta t \cdot \left(\underline{\underline{K}}' \cdot \underline{T}\right)^{(m+\theta)} - \Delta t \cdot \underline{q}^{(m+\theta)} - \Delta t \cdot \underline{f}^{(m+\theta)} = \underline{0}\,, \tag{20}$$

where the linear operator $(\cdot)^{(m+\theta)} \equiv (1-\theta)\,(\cdot)^{(t=t^{(m)})} + \theta\,(\cdot)^{(t=t^{(\ell)})}$, $\ell = (m+1)$, $\underline{\underline{M}}$ and $\underline{\underline{K}}'$ are the local mass and stiffness matrix respectively. Thus the local Jacobian is given by:

$$\underline{\underline{\mathcal{J}}}_e^{(T_h)} = \frac{\partial \underline{\mathcal{R}}_e^{(T_h)}}{\partial \underline{T}^{(\ell)}} = \underline{\underline{M}} + \frac{\partial}{\partial \underline{T}^{(\ell)}}\left(\underline{\underline{K}}' \cdot \underline{T}\right)^{(t^{(\ell)})} \tag{21}$$

this equation yields once again:

$$\underline{\underline{\mathcal{J}}}_e^{(T_h)} = \underline{\underline{M}} + \Delta t \cdot \left(\underline{\underline{K}}' + \delta \underline{\underline{K}}'\right)$$

We assume a linear gradient for thermal conductivity, $\kappa\,(T) = (a \cdot T + b)$; $a, b \in \mathbb{R}$, so that we can benchmark our results from those reported by Hughes [61]. However, we realize that for porous media rocks, the actual relation is proportional to the inverse of this last one, i.e., $\kappa\,(T) \propto (a \cdot T + b)^{-1}$ (see, for instance, [46, 59]). For the simple linear relation, we have:

$$\delta \underline{\underline{K}}' = \sum_p \frac{\partial K'_{ip}}{\partial T_j^{(\ell)}} \cdot T_p^{(\ell)}\,, \tag{22}$$

where the variation term is given by:

$$\frac{\partial K'_{ip}}{\partial T_j^{(\ell)}} = \int_{\Omega^e} a \psi_j \left(\nabla \psi_i\right)^T \cdot \nabla \psi_p \cdot dx\,. \tag{23}$$

We assemble the global tensors, i.e., $\underline{\underline{\mathcal{J}}}^{(T_h)}$ and $\underline{\mathcal{R}}^{(T_h)}$, by direct stiffness summation that utilizes a mapping from local-to-global DOF, i.e., a connectivity table for the elements. We then iterate with the Newton-Raphson algorithm to solve the linearized system of equations in every timestep, namely,

$$\begin{cases} \underline{\underline{\mathcal{J}}}^{(T_h)} \cdot \underline{\Delta T}^{(\ell)} & = \underline{\mathcal{R}}^{(T_h)} \\ \underline{T}^{\ell} & = \underline{T}^{m} - \underline{\Delta T}^{(\ell)}\,. \end{cases} \tag{24}$$

We utilize the same continuous FE space that we described for the elasticity part. Next section covers the Gauss-Newton algorithm with MOR.

3 Proposed MOR method

We introduce here the regularized Petrov-Galerkin Newton-Raphson (PGNR) algorithm. We start with the global MOR algorithm and then comment about obtaining an oblique subspace via POD. Since we consider staggered one-way coupled systems here, i.e., we do not solve all variables simultaneously; we present a general treatment that segregates the primary variables, namely, pressure, temperature, and displacements. We create separate POD basis for every variable and refer to a generic variable, namely, $\xi \in \{u_h, p_h, T_h\}$, which indicates the FE approximation of those quantities.

3.1 Global MOR algorithm

After discretizing the governing Eqs. (1), (4), and (17), we end up with a parametrized nonlinear dynamic computational model described by the large-scale system of algebraic equations denoted by $\underline{\mathcal{R}}^{(\xi)}$:

$$\underline{\mathcal{R}}^{(\xi)}(\underline{\xi}^{(m+1)}; \underline{\xi}^{(m)}; \ldots; \underline{\xi}^{(0)}; \underline{\chi}_{\xi}) = \underline{0}\,, \tag{25}$$

here $\underline{\xi}^{(q)}, q = 0, \ldots, (m+1)$ are succesive timesteps and only $\underline{\xi}^{(m+1)}$ is unknown, $\underline{\xi}^{(q)} \in \mathbb{R}^{N^{(\xi)}}$ are the solutions to Eq. (25). Herein, $N^{(\xi)}$ is the number of unknown degrees of freedom (DOF) for every variable, i.e., the nonlinear system rank, $\underline{\chi}_{\xi} \in \mathbb{R}^{d_{\xi}}$ is the vector of input parameters such as material properties, initial condition and BCS, etc. For the problems of interest here, the function $\underline{\mathcal{R}}^{(\xi)}$:$\mathbb{R}^{N^{(\xi)}} \times \mathbb{R}^{d_{\xi}} \rightarrow \mathbb{R}^{N^{(\xi)}}$ is nonlinear respect to its first argument.
The Jacobian $\underline{\underline{\mathcal{J}}}^{(\xi)}$ of the nonlinear system $\underline{\mathcal{R}}^{(\xi)}$ is defined by a matrix of $N^{(\xi)} \times N^{(\xi)}$ partial derivatives

$$\mathcal{J}_{ij}^{(\xi)} \equiv \frac{\partial \mathcal{R}_i^{(\xi)}}{\partial \xi_j^{(m+1)}}\,; i, j = 1, \ldots, N^{(\xi)}\,. \tag{26}$$

Model reduction aims at projecting Eqs. (25) and (26) to a smaller subspace spanned by the solution snapshots on Eqs. (16) and (24). Many implementations have been investigated for reservoir simulation, i.e., single-phase flow as in Eq. (1), and in recent years, they have been extended to multiphase flow by [33, 35, 58, 63]. In the particular case of solving the nonlinear system of equations, as shown above, we employ the Newton-Raphson approach, and we know that it is a local method. Thus, its convergence relies on the choice of an initial point. Providing an appropriate initial guess for a given problem may be cumbersome, so we develop a modified strategy to the Newton iteration by adding a globalization strategy to improve robustness. The line-search procedure below seeks convergence regardless of the initial point. Towards this end, we introduced a suitable merit function in [21], which guarantees that Newton's direction aims at a solution:

$$M(\tilde{\underline{\xi}}) = ||\underline{\mathcal{R}}^{(\xi)}(\Phi(\tilde{\underline{\xi}}))||^2, \quad \Phi(\tilde{\underline{\xi}}) = \underline{\xi}_o + \underline{\underline{L_{\xi}}}^T \tilde{\underline{\xi}}, \quad \tilde{\underline{\xi}} \in \mathbb{R}^{\tilde{n}^{(\xi)}}\,. \tag{27}$$

here $\underline{\underline{L_{\xi}}}^T \in \mathbb{R}^{N^{(\xi)} \times \tilde{n}^{(\xi)}}$ is the subspace matrix and $\tilde{n}^{(\xi)}$ is the reduced space dimension. From here on, the notation $\tilde{(\cdot)}$ refers to variables in the reduced space. The PGNR algorithm proposed in [20, 21] yields: find

$\underline{\xi} \in \mathbb{R}^{N^{(\xi)}}$, $\underline{\mathcal{R}}^{(\xi)}(\underline{\xi}) = \underline{0}$. The next two subsections introduce the Levenberg-Marquardt regularization and the resulting Petrov-Galerkin Newton-Raphson algorithm that we employ for both our full order and reduced models.

3.1.1 Levenberg-Marquardt regularization

It is well-known that both the singularity of $\underline{\underline{\mathcal{J}}}^{(\xi)}$ and the high nonlinearity of $\underline{\mathcal{R}}^{(\xi)}$ impact the performance of the Newton method. To lessen these drawbacks, we rediscover two standard regularization types [3, 21]: the first one deals with an eventual near-singularity of $\underline{\underline{\mathcal{J}}}^{(\xi)}$, while the second one tackles the high nonlinearities of the components of $\underline{\mathcal{R}}^{(\xi)}$. It is thus desirable to move the smaller eigenvalues of the Jacobian away from zero. We accomplish this goal by using the Levenberg-Marquart regularization [34, 48], which consists of solving the following minimization problem for $\underline{\tilde{\xi}} \in \mathbb{R}^{\tilde{n}^{(\xi)}}$:

$$\min_{\underline{\tilde{\xi}} \in \mathbb{R}^{\tilde{n}^{(\xi)}}} \left\{ ||\underline{\underline{L_\xi}}^T \underline{\xi} + \underline{\underline{\mathcal{J}}}^{(\xi)^{-1}} \underline{\mathcal{R}}^{(\xi)}||^2_{\underline{\underline{\mathcal{J}}}^{(\xi)^T} \underline{\underline{\mathcal{J}}}^{(\xi)}} + \frac{\varrho}{2} ||\underline{\underline{L_\xi}}^T \underline{\xi}||^2_{\underline{\underline{\mathcal{J}}}^{(\xi)^T} \underline{\underline{\mathcal{J}}}^{(\xi)}} + \frac{\iota}{2} ||\underline{\xi}||^2 \right\}, \tag{28}$$

The solution is given by [3, 20, 21] (see these references for full development):

$$(\underline{\underline{\Psi_\xi}}^T \underline{\underline{\Psi_\xi}} + \iota \mathbf{I}) \cdot \Delta \underline{\tilde{\xi}} = -\underline{\underline{\Psi_\xi}}^T \frac{\underline{\mathcal{R}}^{(\xi)}}{1 + \varrho ||\underline{\mathcal{R}}^{(\xi)}||}; \tag{29}$$

where $\underline{\underline{\Psi_\xi}} = \underline{\underline{\mathcal{J}}}^{(\xi)} \cdot \underline{\underline{L_\xi}}^T$. The term $\iota \mathbf{I}$ avoids the singularity while the factor $\left(1 + \varrho ||\underline{\mathcal{R}}^{(\xi)}||\right)^{-1}$ decreases the Lipchitz constant of $\underline{\mathcal{R}}^{(\xi)}$, $\varrho \in (0, 1)$.

3.1.2 Petrov-Galerkin Newton-Raphson (PGNR) algorithm

We enumerate the high-level steps below and provide the resulting algorithm next.

1) Petrov-Galerkin direction Eq. (29).
2) Petrov-Galerkin Newton-Raphson step (decompression): $\Delta \underline{\xi} = \underline{\underline{L_\xi}}^T \Delta \underline{\tilde{\xi}}$.
3) Sufficient decrease (globalization): Find $\varsigma \in (0, 1]$:

$$||\underline{\mathcal{R}}^{(\xi)}(\underline{\xi} + \varsigma \Delta \underline{\xi})|| < g(\varsigma) ||\underline{\mathcal{R}}^{(\xi)}(\underline{\xi})||, \qquad g(\varsigma) < 1.$$

4) Update: $\underline{\xi} = \underline{\xi} + \varsigma \Delta \underline{\xi}$.

We remark that this is a global algorithm that retains its q-quadratic rate of convergence moving on the affine subspace $\underline{\xi}_0 + \underline{\underline{L_\xi}}^T \underline{\tilde{\xi}}, \tilde{n}^{(\xi)} \ll N^{(\xi)}$. We present the algorithm's pseudo-code below. Notice that for linear elasticity the residual and Jacobian reduce to (see Eq. (16)):

$$\begin{aligned} \underline{\mathcal{R}}^{(u_h)} &= \underline{\underline{K}} \cdot \underline{u}^{(k+1)} - f_u + \underline{\underline{Q}} \left(\underline{p}^{(k)} - \underline{p}^{(0)} \right) \\ \underline{\underline{\mathcal{J}}}^{(u_h)} &= \underline{\underline{K}} \,. \end{aligned} \tag{30}$$

In Algorithm 1 for simplicity, we take $\iota = \varrho ||\underline{\mathcal{R}}^{(\xi)}(\underline{\xi}^{(k)})||$. We employ as stopping criteria for the algorithm the norm of the residual, $\delta_k = \|\underline{\mathcal{R}}^{(\xi)}(\underline{\xi}^{(k)})\|$, the maximum number of iterations, and the difference between two successive iterations, $\epsilon_k = \|\underline{\xi}^{(k)} - \underline{\xi}^{(k-1)}\|$. We require that these metrics lie below their tolerances, i.e., ϵ^{TOL} and δ^{TOL}, and not exceeding a certain number of allowed iterations K^{Max}. The algorithm also requires additional configuration flags such as $bMOR$, $bRegld = (bRegld1 || bRegld2)$, and $bLSearch$. If $bMOR$ is true, then we need to provide a projection matrix $\underline{\underline{L_\xi}}^T$. The functions $ResidualJacobian()$ and $Jacobian()$ evaluate, for the specific problem, the residual and the Jacobian of the nonlinear system. Similarly, the function $LineSearch()$, implements the line-search algorithm that is explained in [20].

3.2 Proper Orthogonal Decomposition

As in the standard POD approach, we ensemble the matrix $\underline{\underline{\Theta}}^{(\xi)}$ with the set of snapshots $\underline{\xi}^{(j)} \in \mathbb{R}^{N^{(\xi)}}$ as column vectors, $j = 1, \ldots, N^s$, where N^s is the number of them. Notice that we assume, without generality loss, that we have an equal number of snapshots for every variable at the same time stations.

$$\underline{\underline{\Theta}}^{(\xi)} = \left[\left(\underline{\xi}^{(1)} - \hat{\underline{\xi}} \right) \left(\underline{\xi}^{(2)} - \hat{\underline{\xi}} \right) \ldots \left(\underline{\xi}^{(N^s)} - \hat{\underline{\xi}} \right) \right], \tag{31}$$

we take the singular value decomposition (SVD) of $\underline{\underline{\Theta}}^{(\xi)}$:

$$\underline{\underline{\Theta}}^{(\xi)} = \underline{\underline{U_\xi}} \cdot \underline{\underline{\Sigma_\xi}} \cdot \underline{\underline{V_\xi}}^T = \underline{\underline{U_\xi}} \cdot \begin{bmatrix} \zeta_1^{(\xi)} & \ldots & 0 \\ \vdots & \ddots & \vdots \\ 0 & \ldots & \zeta_{N^s}^{(\xi)} \\ 0 & \ldots & 0 \end{bmatrix} \cdot \underline{\underline{V_\xi}}^T, \tag{32}$$

where $\underline{\underline{U_\xi}} \in \mathbb{R}^{N^{(\xi)} \times N^{(\xi)}}$, $\underline{\underline{\Sigma_\xi}} \in \mathbb{R}^{N^{(\xi)} \times N^s}$, $\underline{\underline{V_\xi}} \in \mathbb{R}^{N^s \times N^s}$, and the singular values $\zeta_1^{(\xi)}, \cdots, \zeta_{N^s}^{(\xi)} \in \mathbb{R}$ and ensemble's mean vector $\hat{\underline{\xi}}$, is computed as:

$$\hat{\underline{\xi}} = \frac{1}{N^s} \sum_{j=1}^{N^s} \underline{\xi}^{(j)} \,. \tag{33}$$

Algorithm 1 PGNR algorithm.

Data: $\underline{\xi} = \underline{\xi}^0$, ϵ^{TOL}, δ^{TOL} and K^{MAX}, $bMOR$ and $\underline{\underline{L_\xi}}^T$, $bRegld_i$, $bLSearch$

Result: Solution to $\underline{\mathcal{R}}^{(\xi)}(\underline{\xi}) = \underline{0}$ or error message

$\epsilon = 1.0, \varsigma = 1.0, \delta = 1.0, k = 0, bRegld = (bRegld1 || bRegld2)$;
while $((\epsilon > \epsilon^{TOL}) \parallel (\delta > \delta^{TOL}))\&\&(k < K^{MAX})$ **do**
  if *(k==0)* **then**
    $[\underline{\mathcal{R}}^{(\xi)}, \underline{\underline{\mathcal{J}}}^{(\xi)}] = ResidualJacobian(\underline{\xi})$;
  else
    $\underline{\underline{\mathcal{J}}}^{(\xi)} = Jacobian(\underline{\xi})$;
  if $bMOR$ **then**
    $\underline{\underline{\Psi_\xi}} = \underline{\underline{\mathcal{J}}}^{(\xi)} \cdot \underline{\underline{L_\xi}}^T$,
    $\Delta\underline{\xi} = \left(\underline{\underline{\Psi_\xi}}^T \cdot \underline{\underline{\Psi_\xi}}\right)^{-1} \cdot \left(\underline{\underline{\Psi_\xi}}^T \cdot \underline{\mathcal{R}}^{(\xi)}\right)$;
    $\Delta\underline{\xi} = \underline{\underline{L_\xi}}^T \cdot \Delta\underline{\xi}$;
  else
    if $bRegld$ **then**
      $\iota = \varrho ||\underline{\mathcal{R}}^{(\xi)}||$;
      if $bRegld1$ **then**
        $\underline{\underline{\mathcal{J}}}^{(\xi)} = \underline{\underline{\mathcal{J}}}^{(\xi)} + \iota \mathbf{I}$;
      if $bRegld2$ **then**
        $\underline{\mathcal{R}}^{(\xi)} = \frac{\underline{\mathcal{R}}^{(\xi)}}{1+\iota}$;
    $\Delta\underline{\xi} = \left(\underline{\underline{\mathcal{J}}}^{(\xi)}\right)^{-1} \cdot \underline{\mathcal{R}}^{(\xi)}$;
  if $bLSearch$ **then**
    $[\varsigma, \underline{\mathcal{R}}^{(\xi)}] = LineSearch(\underline{\xi}, \Delta\underline{\xi}, \underline{\mathcal{R}}^{(\xi)})$;
  $\underline{\xi} = \underline{\xi} - \varsigma\Delta\underline{\xi}$;
  if $bMOR$ **then**
    $\delta = ||\underline{\underline{\Psi_\xi}}^T \cdot \underline{\mathcal{R}}^{(\xi)}||$;
  else
    $\delta = ||\underline{\mathcal{R}}^{(\xi)}||$;
  $\epsilon = \varsigma \cdot ||\Delta\underline{\xi}||, k = k + 1$;
if $(k < K^{MAX})$ **then**
  return $\underline{\xi}$;
else
  print "Could not converge...";

If we represent problem (16) with a reasonable number of snapshots from which a proper set of basis vectors is available, the singular values decrease rapidly, so only a limited number of basis vectors are necessary to approximate the snapshots as they preserve the most important ensemble's energy contribution. To create a POD basis, we truncate the basis vector by considering:

$$\tilde{n}^{(\xi)} \leq N^s \Rightarrow \frac{\sum_{j=1}^{\tilde{n}^{(\xi)}} \left(\zeta_j^{(\xi)}\right)^2}{\sum_{j=1}^{N^s} \left(\zeta_j^{(\xi)}\right)^2} \geq \varepsilon_\xi^e \,. \tag{34}$$

Above ε_ξ^e is a pre-defined energy threshold. If the latter is high, say over 99% of the total energy, then $\tilde{n}^{(\xi)}$ modes accurately capture the principal features and reconstruct the dataset approximately. Thus, we form a reduced subspace, which only spans:

$$\underline{\underline{L_\xi}}^T = \left[\, \underline{U_\xi}^{(1)} \;\; \underline{U_\xi}^{(2)} \;\; \ldots \;\; \underline{U_\xi}^{(\tilde{n}^{(\xi)})} \,\right] , \tag{35}$$

where $\underline{U_\xi}^{(j)}$ are the columns of $\underline{\underline{U_\xi}}$. We finalize defining the following percentage compression ratios (CR) for POD and MOR:

$$\begin{aligned} \tau_{\text{POD}}^{(\xi)} &= 100 \cdot \left(1 - \left(\tfrac{\tilde{n}^{(\xi)}}{N^S}\right)\right) , \\ \tau_{\text{MOR}}^{(\xi)} &= 100 \cdot \left(1 - \left(\tfrac{\tilde{n}^{(\xi)}}{N^{(\xi)}}\right)\right) . \end{aligned} \tag{36}$$

Notice that the number of DOF, $N^{(\xi)}$, does not include those points in the domain with prescribed Dirichlet BCS. We usually do not consider them since their information is often redundant among the snapshots. Also, we mostly assemble both the residual and Jacobian only for the unknows DOF as is common in standard FE procedures.

3.3 Local vs. global POD: time partitioning

We refer to POD with time partitioning as LPOD. Indeed, we partition the time interval of interest into several subintervals as shown in Fig. 1, where we cluster together the snapshots that lie in every reduced order basis (**ROB**) time's window. The partitioning is, in general, arbitrary but depends on the system dynamics, for instance, changing regimes or rapid transients that we wish to capture separately. The ROB intervals may overlap for the offline stage (back-tracking in time), but they don't in the online phase (double-lines). In the later stage, for a given time, we pick up only one ROB exclusively. We then perform the POD analysis in Section 3.2 in every ROB independently. LPOD renders smaller projection basis than a global-in-time approach and also retains more energy in the sense that adding the local basis modes up often results in larger oblique subspace dimension $\tilde{n}^{(\xi)}$.

Let nROBs be the number of time intervals whose limits are $[t_0, t_1, \ldots, t_{\text{nROBs}}]$. **BCS**$(t)$ represent boundary conditions that can vary as a function of time. Algorithm 2 corresponds to the offline stage for a given nonlinear model problem. Once we define the time partitioning, we

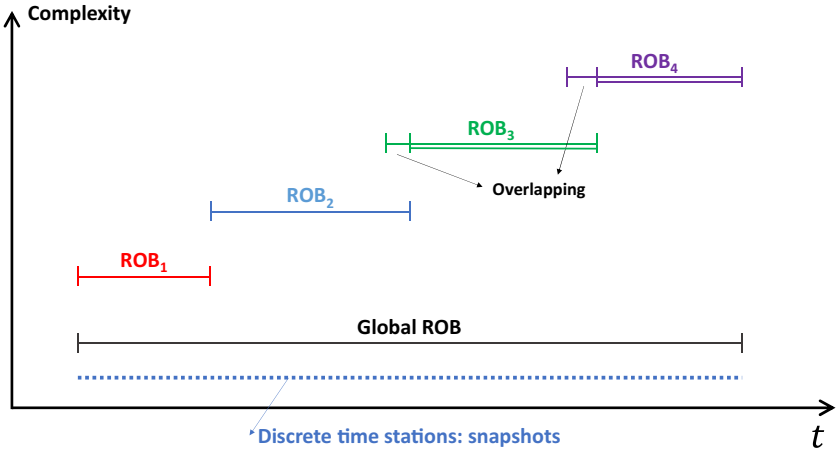

Fig. 1 A depiction of POD with time partitioning

can execute the MOR stages, for which the time intervals remain constant. vROBs represent an array of ROBs, for which every entry refers to a given time interval, i.e., ROB_i: $t \in [t_i, t_{i+1}]$. In line 2, we allocate memory to store the snapshots in every ROB, while in line 6, the function CopySnpshtCol copies $\underline{\xi}^{(m+1)}$ to the given ROB dependent if t lies within its interval. After collecting all snapshots, we perform POD analysis in every ROB independently. Since the sizes of the local snapshot matrixes are smaller than an equivalent global-in-time matrix, often, LPOD alleviates the SVD in the sense that the runtime to execute step 8 is shorter than a global approach.

Algorithm 2 Offline stage for LPOD.

Data: nROBs, $[t_0, t_1, \ldots, t_{\text{nROBs}}]$, $\mathbf{BCS} = \mathbf{BCS}(t)$
Result: LPOD basis

1 $\underline{\xi}^{(0)}, \Delta t^{(0)}$ = initialCondition(<static model>);
/* Initialization */
2 $m = 0, t = \Delta t = \Delta t^{(0)}$, vROBs.AllocateSnpShts($N^{(\xi)}$);
/* Time stepping loop */
3 **while** $(t < t_{max})$ **do**
/* Interpol inputs at this time */
4 $\mathbf{BCS}_m$ = InterpolBCS(t);
/* Solve the nonlinear problem with algorithm 1, no MOR */
5 $\left[\underline{\xi}^{(m+1)}\right]$ = solveNR($t, \underline{\xi}^{(m)}, \mathbf{BCS}_m$);
/* Seek ROB and copy data */
6 vROBs.CopySnpshtCol($t, m, \underline{\xi}^{(m+1)}$);
/* Update */
7 $t = t + \Delta t, m = m + 1$;
/* Perform POD analysis in every ROB (see Section 3.2) */
8 vROBs.BuildPODBasis($[\varepsilon^e, \ldots, \varepsilon^e]$);

Algorithm 3 represents the online stage for LPOD. What is relevant here is step 5 in which the function GetTimeInt seeks the local ROB that corresponds to the current time and returns its oblique subspace basis. Also, we remark that LPOD impacts how we compute the root-mean-square error since it also requires seeking the given ROB in function CmpSnpshtColErr (see the next section for the proper error definition.)

Algorithm 3 LPOD's online stage.

Data: nROBs, $[t_0, t_1, \ldots, t_{\text{nROBs}}]$, $\mathbf{BCS} = \mathbf{BCS}(t)$
Result: ROM approximation

1 $\underline{\xi}^{(0)}, \Delta t^{(0)}$ = initialCondition(<static model>);
/* Initialization */
2 $m = 0, t = \Delta t = \Delta t^{(0)}$, dRMSerr = 0;
/* Time stepping loop */
3 **while** $(t < t_{max})$ **do**
/* Interpol inputs at this time */
4 $\mathbf{BCS}_m$ = InterpolBCS(t);
/* Seek ROB and grab Modes */
5 $\left[\underline{\underline{L_\xi}}^T\right]$ = vROBs.GetTimeInt(t);
/* Solve the nonlinear problem with algorithm 1, MOR is enabled */
6 $\left[\underline{\xi}^{(m+1)}\right]$ = solvePGNR($t, \underline{\xi}^{(m)}, \mathbf{BCS}_m, \underline{\underline{L_\xi}}^T$);
/* Accumulate errors */
7 dRMSerr = dRMSerr + vROBs.CmpSnpshtColErr($t, m, \underline{\xi}^{(m)}$);
/* Update */
8 $t = t + \Delta t, m = m + 1$;
/* Compute rms-error */
9 dRMSerr = sqrt(dRMSerr / $(N^{(\xi)} \cdot N^s)$);

4 Numerical examples

The authors implemented these FE models in the Integrated Parallel Finite Element Analysis program (*IPFA*) that is a C++ application whose main characteristics are described in [16, 28, 29]. IPFA employs standard continuous Lagrange polynomials as shape functions for the space discretization. All examples herein were run on a MacBook Pro laptop equipped with an Intel(R) Quad-Core(TM) i7-4870HQ CPU @ 2.5GHz and 16 GB of RAM. All numerical simulations reported below utilized ILU as preconditioner and conjugate gradient as the iterative solver. Visualizations are performed with the "LogProc" application (see also www.logproc.com).

Given the matrix $\underline{\underline{\Lambda}}^{(\xi)} \in \mathbb{R}^{N^{(\xi)} \times N^s}$, we define the root-mean-square norm (rms) as:

$$\left\| \underline{\underline{\Lambda}} \right\|_{rms}^{(\xi)} = \sqrt{\frac{1}{N^{(\xi)} \cdot N^s} \sum_{i=1}^{N^{(\xi)}} \sum_{j=1}^{N^s} \left(\Lambda_{ij}^{(\xi)} \right)^2} \; ; \Lambda_{ij}^{(\xi)} = |\xi_{i\ (\mathrm{FOM})}^{j} - \xi_{i\ (\mathrm{ROM})}^{j}| \,, \tag{37}$$

and we employ this definition to compute the error between FOM and ROM for transient problems, where i refers to spatial discretization while j implies snapshots in time. We present four one-way and one coupled numerical examples; the first one covers nonlinear heat transfer and elasticity. The second example couples a black-oil reservoir (RS) simulation with mechanics but we only input the pressures exported from a commercial simulator. The third example focuses on single-phase flow for an unconventional RS in which we reduce both physics to obtain substantial speedups. The fourth example tackles the role of the heterogeneity in the reduction process as well as a more realistic case with a lot more DOF. Finally, we present preliminary numerical results for a standard two-way benchmark poroelastic problem, namely Mandel's problem.

4.1 Example 1: arch problem

We revisit here this interesting heat transfer 2-D problem that we presented in [17, 61], whose distinctive features are the two re-entrant sharp corners where there may be singularities in the solution. The material properties are constant density and specific heat,

$$\rho = 1.0 \mathrm{kg/m^3} \; ; C_p = 1.0 \frac{\mathrm{W \cdot s}}{\mathrm{kg} \cdot^{\circ} \mathrm{K}},$$

and a linear isotropic thermal conductivity,

$$\kappa = \left(1 + \frac{T}{1000^{\circ}\mathrm{K}} \right) \frac{\mathrm{W}}{\mathrm{m} \cdot^{\circ} \mathrm{K}} \,.$$

Figure 2 shows the domain, whose dimensions are 1.0 m × 0.5 m, a sample mesh, and the given BCS, which are of Dirichlet type on the left- and right-most sides, and insulation on all other edges:

$$n \cdot (\kappa \nabla T) = 0.$$

We assume the initial temperature distribution as:

$$T\left(x, y, t^*\right) = 10^3 \mathrm{erfc}\left(\frac{x}{2\sqrt{\kappa t^*}} \right)^{\circ} \mathrm{K},$$

which is the short-time linear solution at a time t^* for a planar semi-infinite medium. In our analysis, we considered $\kappa = 1$ and $t^* = 0.0005$ s in the calculation of our initial conditions.

We assume for the mechanics, linear isotropic elasticity with $E = 30$ Ksi and $v = 0.3$ and the coefficient of thermal dilatation $\beta = 1 \cdot 10^{-5} \mathrm{K}^{-1}$ and the bulk modulus $K = E/(3 \cdot (1 - 2v))$ and plane strain. The bottommost edges are clamped while the others are traction free.

Figure 3 shows temperature field snapshots for different times increasing from top to bottom. FOM results are in the left-column while ROM's absolute error is on the right. We simulate 0.1 s with a fully implicit approach. We consider $\Delta t = 5 \cdot 10^{-3}$ s that renders 21 evenly spaced snapshots. We impose the energy constraint $\varepsilon^e = 1.0 - 10^{-7}$ for temperature, which yields a $\tau_{\mathrm{POD}} = 40\%$ and a τ_{MOR} at least of 99.85%, which is indeed impressive. We observe that a heating front quickly travels from left to right as expected due to the temperature gradient. As a qualitative benchmark, the temperature profile reported by [61] agrees very well with our results. Figure 4 includes a pair of snapshots that depict the induced horizontal displacement field. We see dilatation that grows from the upper-right corner while compression appears from the upper-left corner. Figure 5 shows additional mechanical results that correspond to the mean-stress. This latter depicts the magnitude of the induced thermal stresses.

We assume the more stringent energy constraint of $\varepsilon^e = 1.0 - 10^{-9}$ for the displacements. The number of significant snapshots for mechanics renders $\tau_{\mathrm{POD}} = 31.58$. We run successively refined meshes to asses the performance of our MOR scheme. Table 1 summarizes relevant results for this coupled simulation. The listing includes the number of DOF for every variable, namely, temperature and displacements. As a rule of thumb, displacement DOF duplicate those of temperature, but distinct Dirichlet BCS explain the discrepancy. We highlight the remarkable τ_{MOR} at least of 99.92%, which tends to improve with the more significant

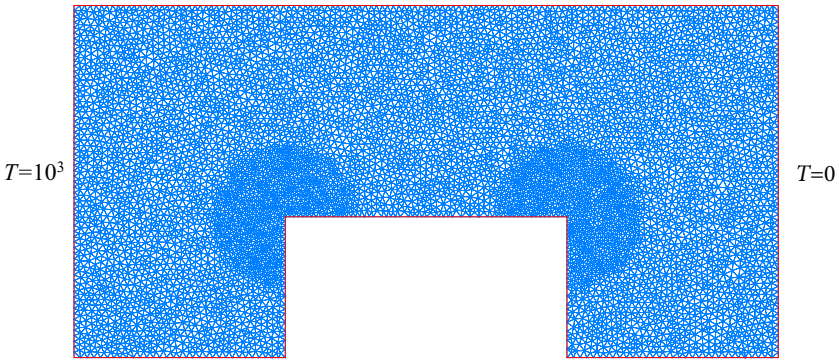

Fig. 2 Mesh, highlighted boundary, and the BCS

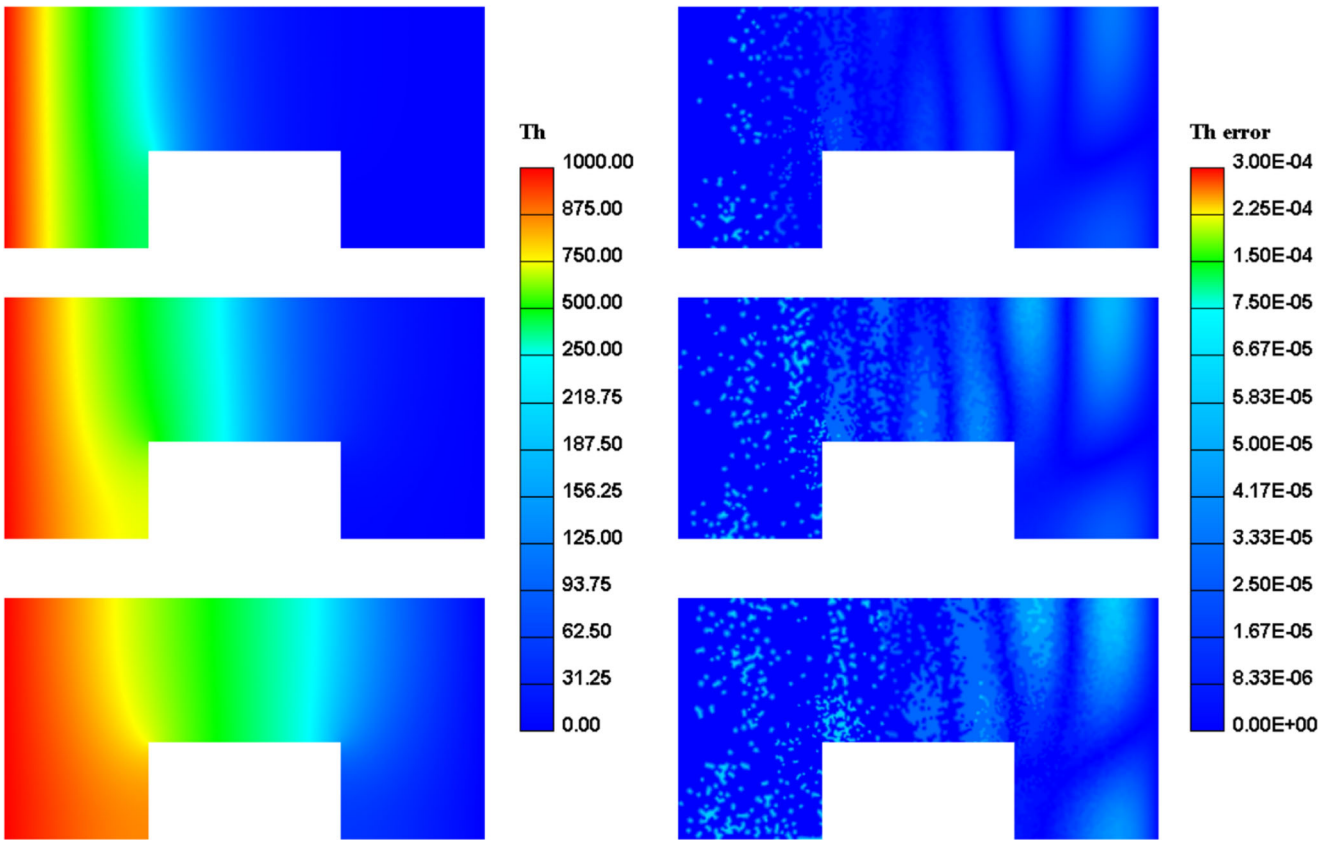

Fig. 3 Solution snapshots, FOM in the left and ROM's error in the right column, $t = 0.025$ s, $t = 0.05$ s, and $t = 0.1$ s, from top to bottom

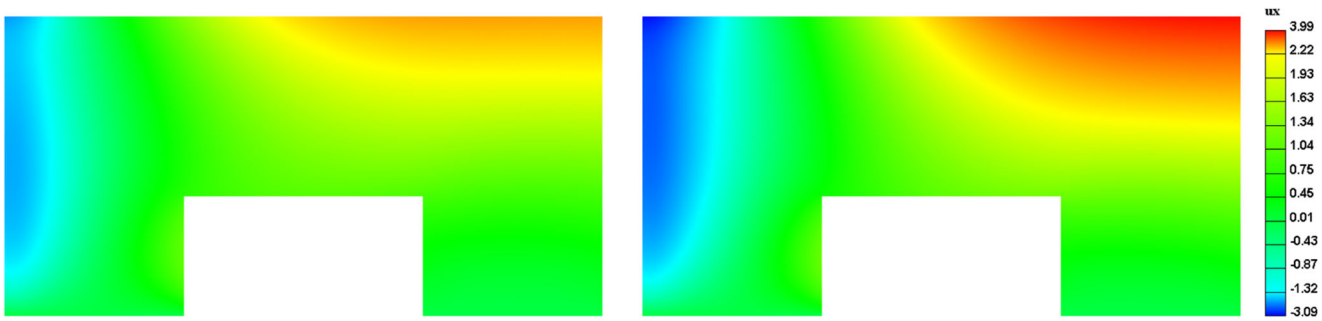

Fig. 4 Horizontal displacement snapshots at $t = 0.05$ s and $t = 0.1$ s, from left to right

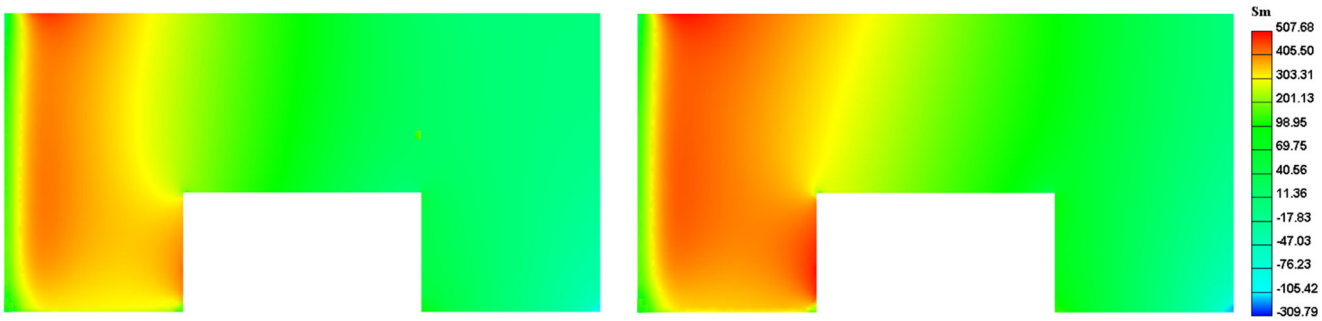

Fig. 5 Mean-stress snapshots at $t = 0.05$ s and $t = 0.1$ s, from left to right

number of DOF. We also reported runtimes for both FOM and ROM. We remark that these times include substantial serial time, for instance, while assembling the Jacobian and Residual for both physics and post-processing to compute stresses. We discuss the origin of the extra serial time in detail below. However, we can still see significant time savings that are better for larger problems as shown. As indicated, we are not far from a $2\times$ speedup for this particular application. Besides the substantial CR, the rms-error, for temperature and displacements, remains neglectable for all cases that we ran. Indeed, MOR achieved smaller errors for mechanics since that problem is linear. Since the temperature front propagates slowly, 20 snapshots were sufficient to reproduce most of the features exhibit herein for both physics. For the other two examples below, we impose the same energy constraint for the mechanics.

Let us focus on the temperature variable to explain the remaining serial time in the simulation. Table 2 highlights the fact that the MOR speedup for energy equation, deteriorates compared to an equivalent linear problem, see [17] for further details. What happens is that we are still assembling the full Jacobian and RHS-vector, for both FOM and ROM, so that part of the runtime remains constant. For problem in Eq. (29), though, we ensemble the Jacobian only once. Now, we face the same challenge in solving the dense linear system in Eq. (30), for instance. To expedite this procedure, one can assemble the Jacobian in parallel, i.e., multi-threading assembling and implement a hyper-reduction technique as we comment in our path forward.

We also profile a model, with a mesh of size of 75K, typical timestep and Table 3 provides relevant time data. Indeed, we realize that most of the runtime goes to assembling the Jacobian and Residual. However, the Petrov-Galerkin step speeds up solving the linear system 3X. We emphasize that systems of this sort in which assembling takes longer that solving are precisely the niche for parallel processing and hyper-reduction techniques such as DEIM [9, 10] and Gappy POD [8, 15].

4.2 Example 2: SPE9 benchmark

We implemented this example through the one-way coupling between the Matlab Reservoir Simulator Toolbox (MRST) [44] and IPFA as we described in [25]. MRST solves the flow equations via a fully implicit approach based cell-centered finite differences while IPFA employs continuous Galerkin finite elements to compute the induced poroelastic displacements and thus stresses. We hooked up both codes by memory through Matlab MEX interface which allows calling native C code from dynamic link libraries. The SPE9 benchmark that was posted by [39] initially to compare black-oil simulators. Figure 6 depicts the porosity field in a grid whose size is $24 \times 25 \times 15$ and has a 10° dipping-angle in the x-direction. The 25 producers initially operate at a maximum rate of 1500 STBO/D, which is lowered to 100 STBO/D from day 300 to 360, and the raised again to its initial value until the end of simulation at 900 days. The single water injector

Table 1 ROM's performance for arch problem

$N^{(T_h)}$	$N^{(u_h)}$	τ_{MOR} [%]	FOM runtime	ROM runtime	$\|\underline{\Delta}\|_{rms}^{(T_h)}$	$\|\underline{\Delta}\|_{rms}^{(u_h)}$
7855	15838	99.92	1 min, 01 s	0 min, 51 s	1.2129e−07	3.8957e−13
31720	63696	99.98	5 min, 10 s	3 min, 30 s	4.1229e−08	2.0200e−13
49761	99778	99.99	8 min, 36 s	5 min, 37 s	1.5314e−07	1.0309e−13

Table 2 MOR's metrics for temperature

$\approx N^{(T_h)}$	FOM runtime	ROM	[MB]
8 K	0 min, 39 s	−3 s	1.2
32 K	2 min, 53 s	−34 s	4.9
50 K	4 min, 51 s	−64 s	7.8

is at a rate of 5000 STBW/D with a maximum bottom-hole pressure of 4000 Psi at reference depth. During the simulation, most of the wells switch from rate control to pressure control (see also https://www.sintef.no/projectweb/mrst/modules/ad-core/spe9/ for further details).

We consider as input 90 oil-pressure snapshots for MOR purposes, i.e., a pressure field every ten days. Figure 7 depicts sample pressure fields, arising from MRST, at different times as indicated. There is a clear depletion scenario in which pressure drops from the top of the RS, which moves to lower parts. We obtain a valid geomechanics mesh by reconstructing the RS model exactly (see [26]), which implies that we extend the flow mesh, and later solving an elasticity problem for mesh generation in which we enforce a constraint to honor the pay-zone exactly so that we project pressure easily, i.e., the identity matrix is the projector. One of the authors proposes such a reconstruction workflow in [19, 22].

In addition to the flow mesh size, we also contemplate Nc = 5, Nu = 5, and No = 7 (Nc refers to mesh patches on the corners and No and Nu stand for over- and under-burden respectively). We extrapolated the RS towards the side-burdens with a factor of 1.0 (RS's length) while we employed 8 (RS's thickness) for the over- and under-burden. Figure 8 plots the resulting geomechanics mesh that encompasses 26,400 elements with 29,172 points. In this cut-away plot, we highlight the fact that we honored the pay-zone mesh precisely as shown in the zoomed in detail. BCS for mechanics is the typical traction-free surface on the top and far-field on all remainder planes. Notice that the far-field BCS implies that the displacement in the perpendicular direction to the given plane is zero. The example also assumes a zero initial displacement field. For the mechanical properties, we assume a layered RS with Young's modulus $E_u = 3 \times 10^4$, $E_p = 1 \times 10^4$, $E_o = 2 \times 10^4$ [Psi], while Poisson's ratio, $v = 0.25$, is constant

Table 3 Profiling: $N^{(T_h)} \approx 75K$ arch problem case

Stage	CPU time
Assembling $\underline{\underline{\mathcal{J}}}^{(T_h)}, \underline{\mathcal{R}}^{(T_h)}$	4s 812ms
Sparselib FOM	0s 46ms
Petrov-Galerkin	0s 15ms

in the whole domain. The subscripts u, p, and o stand for over-burden, pay-zone level and under-burden respectively.

Figure 9 depicts at least three distinct depletion regimes that we observe in the RS. There is an evident depletion in the bottom of the RS; then it depletes the top layers as shown. We attempted to pack all 90 snapshots together, but we later realized that the SVD fails to converge due to an internal error. Our implementation utilizes Armadillo [56], a C++ hyper-templates library that relies on LAPACK to obtain the SVD. The error message in the screen only says that the decomposition failed, but does not provide further details. For instance, authors in [5] state that it is not uncommon that classical methods for computing the SVD of large matrices may fail because they may be ill-suited to handle such cases. Indeed, a global reduced order basis (ROB) is not tractable in this case due to different depletion regimes that are not monotone. We know that the mean-stress will be proportional to the pressure drop in the RS and thus the resulting displacement fields will also be different. The failure has nothing to do with the number of DOF, i.e., memory issue, but instead, the lack of correlation among the displacement snapshots explains why the SVD fails. We could not ensemble more than 24 snapshots together. We thus propose partitioning the time interval into four almost evenly spaced local ROBs (see [2, 17, 32]), every one of which includes about 240 days. We then ran the FOM and captured the local ROBs as explained in Section 3.3; Table 4 summarizes the metrics for this ROM.

We have for all these ROBs, $N^{(u_h)} = 82910$ and $\tau_{\text{POD}} = 0\%$. This ROM could properly reproduce the features of the FOM with an error that is neglectable ($\approx 10^{-14}$). The CR and speedup are substantial as indicated. Indeed, this ROM yields a 14.9× speedup if we consider the runtimes in the table that don't include the assembling time which is about 11 s 202 ms. We employed four threads to assemble the stiffness matrix and post-processing the stresses, which reduces the serial time per timestep.

These MOR results are promising in the sense that for most coupled flow and mechanics problems, solving the sparse system takes longer time than assembling the stiffness matrix. The latter is thus precisely the niche for Petrov-Galerkin MOR. It is also possible to speed up computing the stiffness or Jacobian by combining parallel computing and hyper-reduction techniques, such as DEIM and Gappy interpolation (see [9, 33, 35, 58, 64]). There are other factors that we need to asses such as the influence of heterogeneity and BCS in the reduction process. Finally, Fig. 10 depicts vertical displacement snapshots at 240, 480, 720, and 900 days from left to right and top to bottom. We observe the classical compaction dome that grows from the pay-zone towards the overburden. A build-up also exists in the under-burden. The RS mesh displays pressure at those times as a reference. We see the evident correlation between

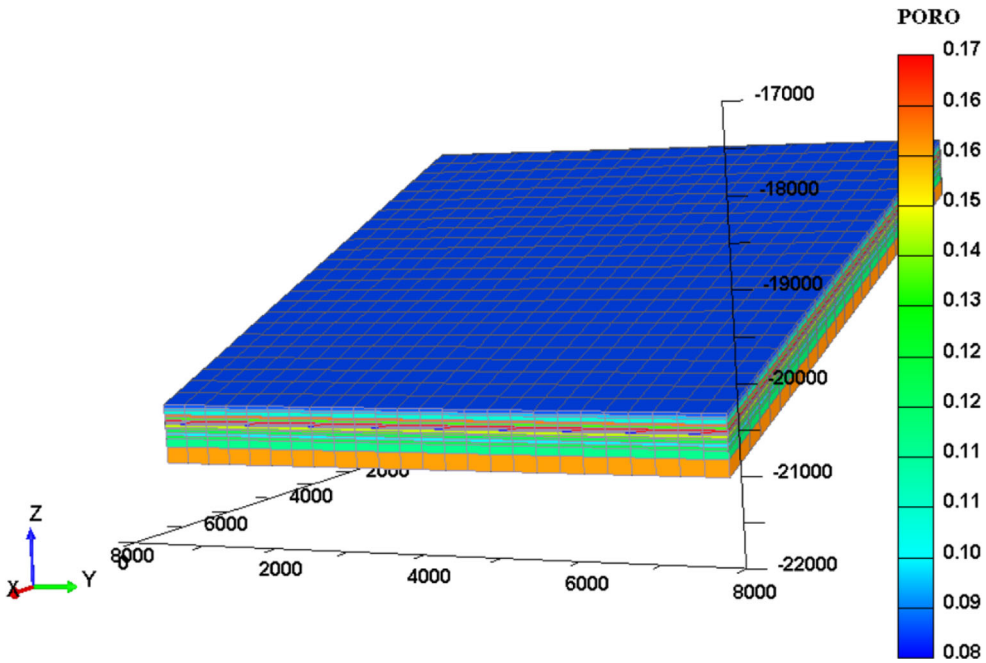

Fig. 6 Porosity field of SPE9 dataset

u_z and the pressure drop in the RS. Also, notice that the scales change with the snapshots as a consequence of the different regimes that we mentioned.

4.3 Example 3: single-phase flow in an unconventional RS

We now focus on a synthetic unconventional RS model whose geometry we show in Figs. 11 and 12. The model consists of two fractured horizontal wells, separated by a distance equal to $2 \cdot s_w$. A uniform pressure p_{bh} is applied along the transverse fractures, which are divided by a distance of s_f. We keep the pressure constant throughout production. The RS is homogeneous, isotropic, and poroelastic and is bounded by layers with similar mechanical properties. Flow only occurs within the RS and does not leak into the surrounding strata. We assume no-flow and far-field BCS for every physics respectively. We considered perfectly transverse fractures in the offset well to simplify the analysis. We also understand that the stresses

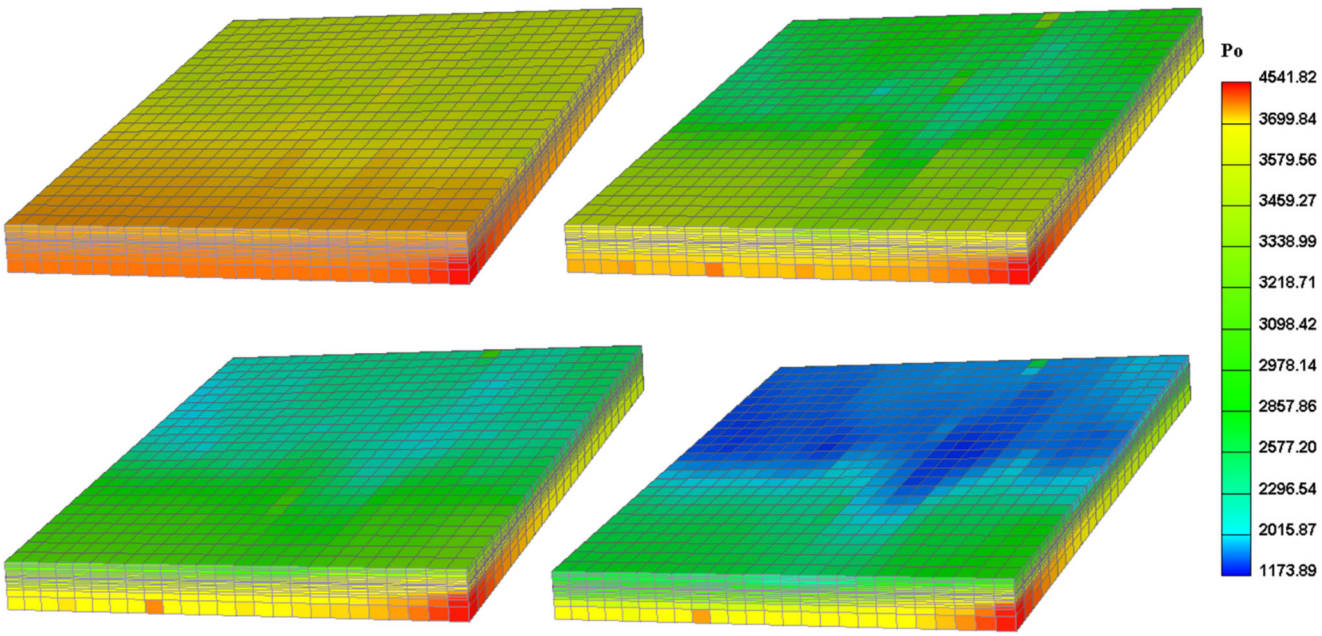

Fig. 7 Pressure snapshots at 0, 200, 400, and 600 days from left to right and top to bottom

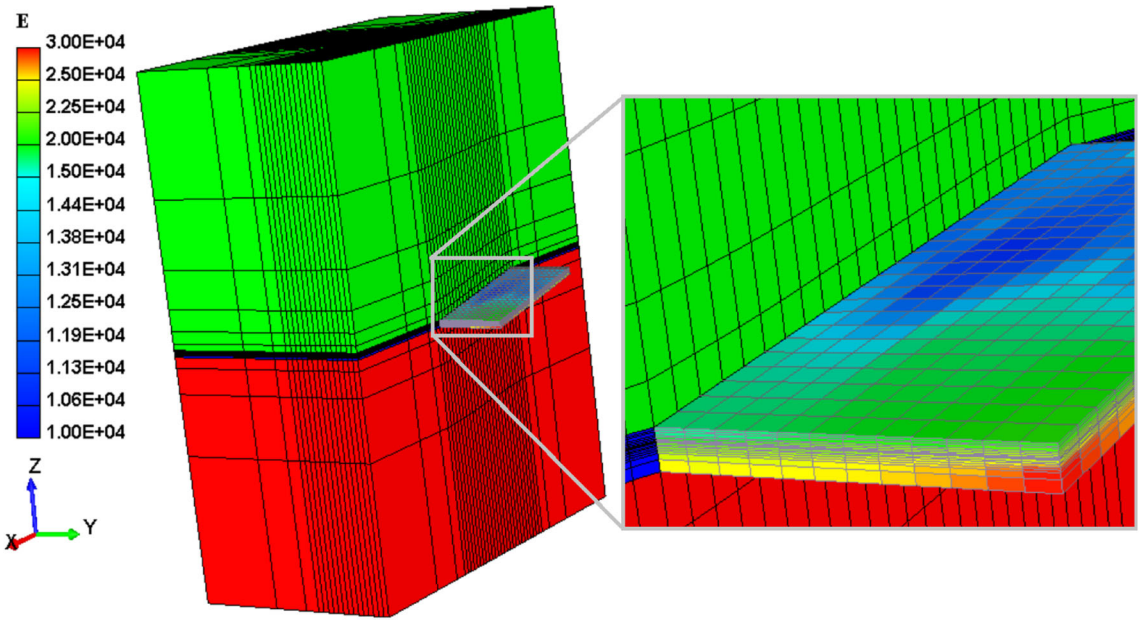

Fig. 8 Reconstructed mechanics' mesh

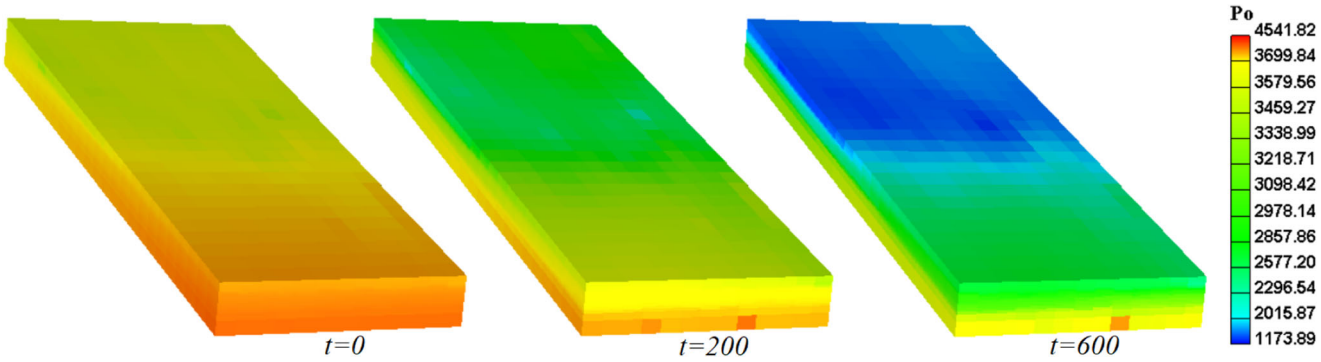

Fig. 9 Pressure drop regimes at different times

Table 4 LPOD's performance for SPE9

ROB	Timesteps	N^s	τ_{MOR} [%]	FOM runtime	ROM runtime	$\|\Delta\|_{rms}^{(u_h)}$
1	1–24	24	99.97	40 s 921 ms	2 s 484 ms	1.5369e−14
2	24–48	24	99.97	36 s 890 ms	2 s 468 ms	4.0049e−14
3	48–72	24	99.97	36 s 703 ms	2 s 546 ms	6.3672e−14
4	72–90	18	99.98	26 s 281 ms	1 s 921 ms	8.9245e−14

Fig. 10 Sample u_z snapshots

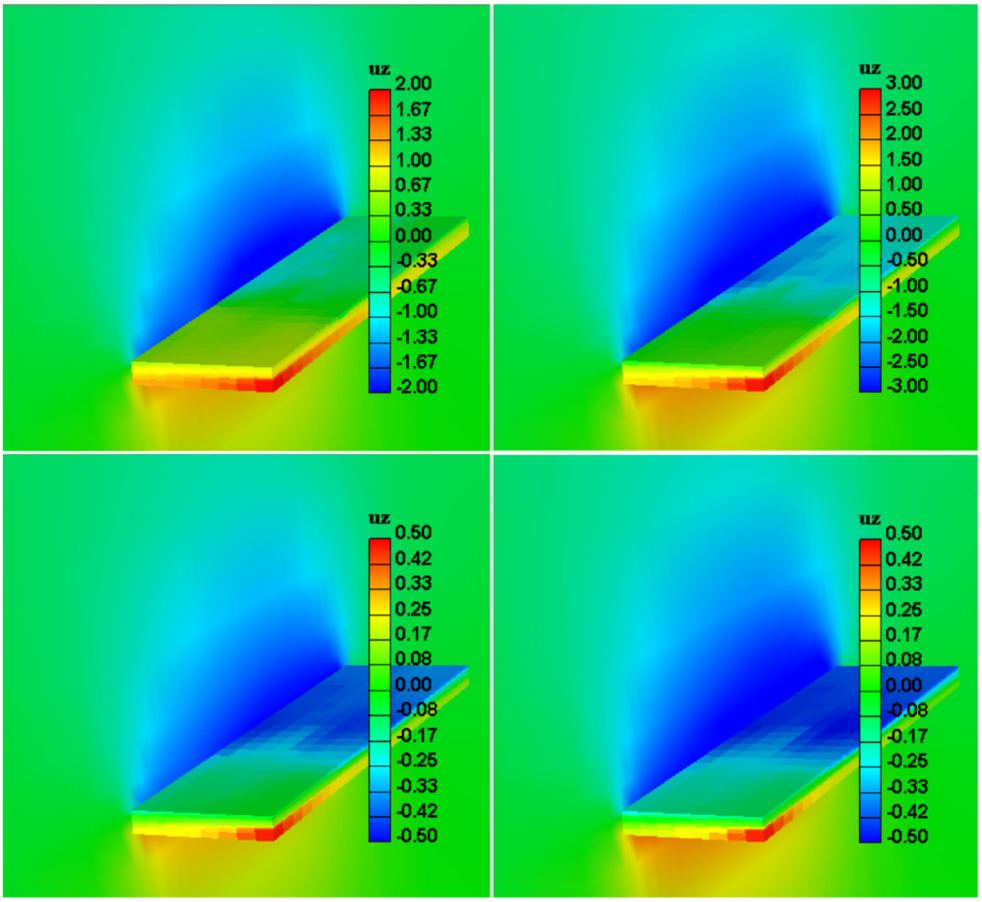

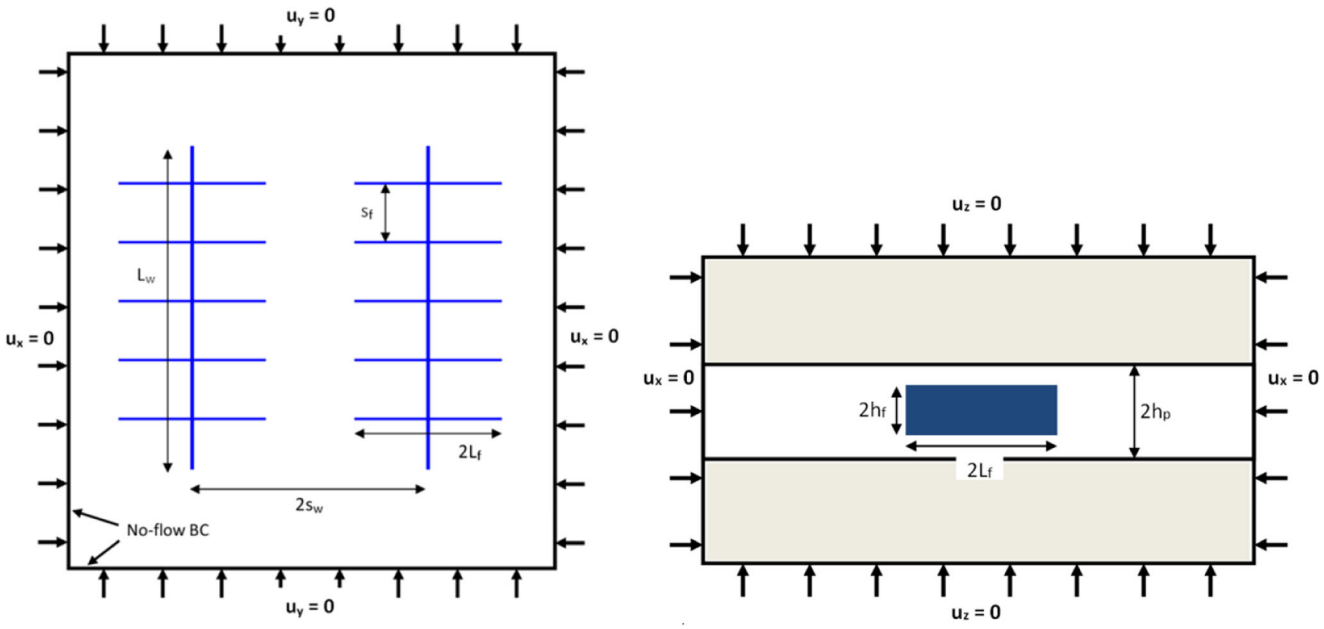

Fig. 11 Geometry and BCS in the horizontal and vertical planes, after [55]

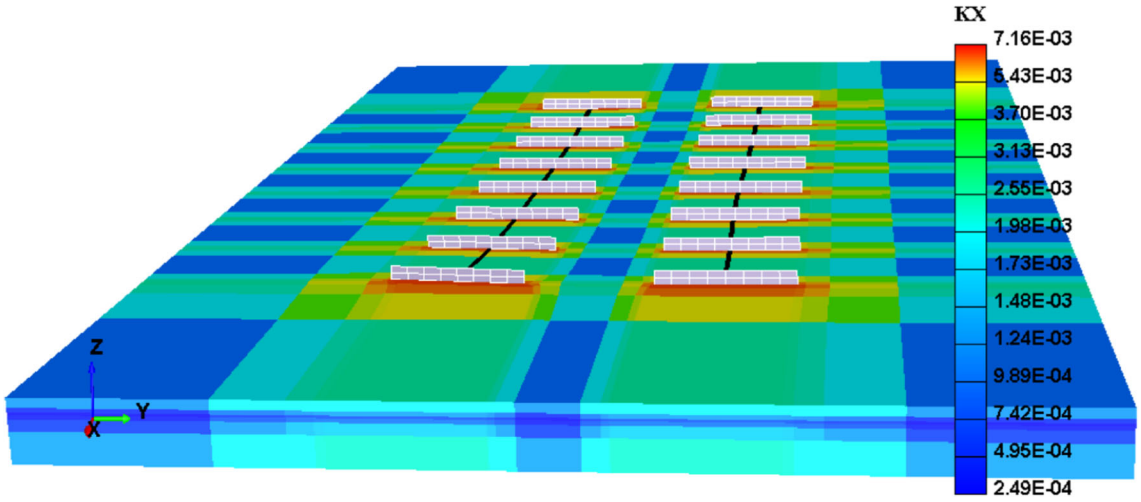

Fig. 12 Sample curvilinear mesh and permeability field

in the infill region are impacted only by poroelastic effects as mentioned by [55]. Table 5 summarizes all relevant parameters for this one-way coupled flow and mechanics simulation that mimics a case representative of liquid-rich shale development. The numerical values for the mechanical properties on this table are similar to those reported by [14, 50] for the Eagle Ford shale play. We previously developed a preprocessor which generates a curvilinear mesh based on the well trajectories and additional geometrical parameters. We are mainly interested herein in varying the number of fractures, that would be equal in each well so that we can obtain a series of more challenging problems to speed up with MOR.

Table 5 Unconventional RS model's parameters

Parameter	Value (unit)
Pay-zone half-height h_p	400 ft
Fracture half-height h_f	50 ft
Fracture half-length L_f	200 ft
Stage spacing s_f	$\approx$ 428, 200, 158 ft
Well length L_w	$\approx$ 3000 ft
Well spacing s_w	$\approx$ 1000 ft
Number of fractures	8, 16, 20
Matrix permeability k_m	0.3 µd
Fracture permeability k_f	10 µd
SRV's permeability k_{SRV}	1.5 µd
Young's modulus E	2000 Ksi
Biot modulus M	850 Ksi
Reservoir pressure p_R	10000 Psi
Bottomhole pressure p_{bh}	7000 Psi
Condensate viscosity μ	0.25 cp
Porosity ϕ	0.05
Poisson's ratio ν	0.2
Biot coefficient α	0.7

Figure 12 depicts a cut-away (upper half) representation that highlights the well trajectories in bold black and the fractures that are planar and perpendicular to well's path. The preprocessor generates a graded mesh and also populates properties by using the same blending rationale. The resulting permeability field is slightly heterogenous to represent the concept of stimulated rock volume (SRV) better. Figure 13 shows a vertical cross-section that emphasizes the fact we are dealing with a general 3-D hexahedral mesh, i.e., it is not extruded as a 2.5-D mesh, and thus the grid deviates in the vertical direction as shown.

For the sake of simplicity, we consider the same domain for flow and mechanics. We ran a series of models with 8, 16 (see Fig. 14), and 20 fractures for 4 years with the fully implicit scheme (16) with a timestep size of a month. We ran all FOM serially to compare with a MOR model that also incorporates multi-threading assembling and post-processing for both flow and mechanics. We employ four threads that in average provide a 4× speedup over the mentioned serial tasks. Notice that we assemble matrixes $\underline{\underline{S'}}$ and $\underline{\underline{K}}$ only once at the initialization, and thus for marching the convolution problem (16), we need to solve those sparse systems in every timestep. Postprocessing, the stresses per iteration, can take up to 3 s that add to the serial time.

Let us comment on the numerical results first. Figure 15 depicts pressure field snapshots after two and four years of production. We observe a reasonably symmetric and monotone depletion scenario where we stimulated the formation only in the vicinity of the fractures due to the very small permeability values. Of course, if we can pack more fractures, we will deplete and thus produce more, which is evident if we compared the models with 16 (left column) and 20 (right column) fractures. We also remark that the

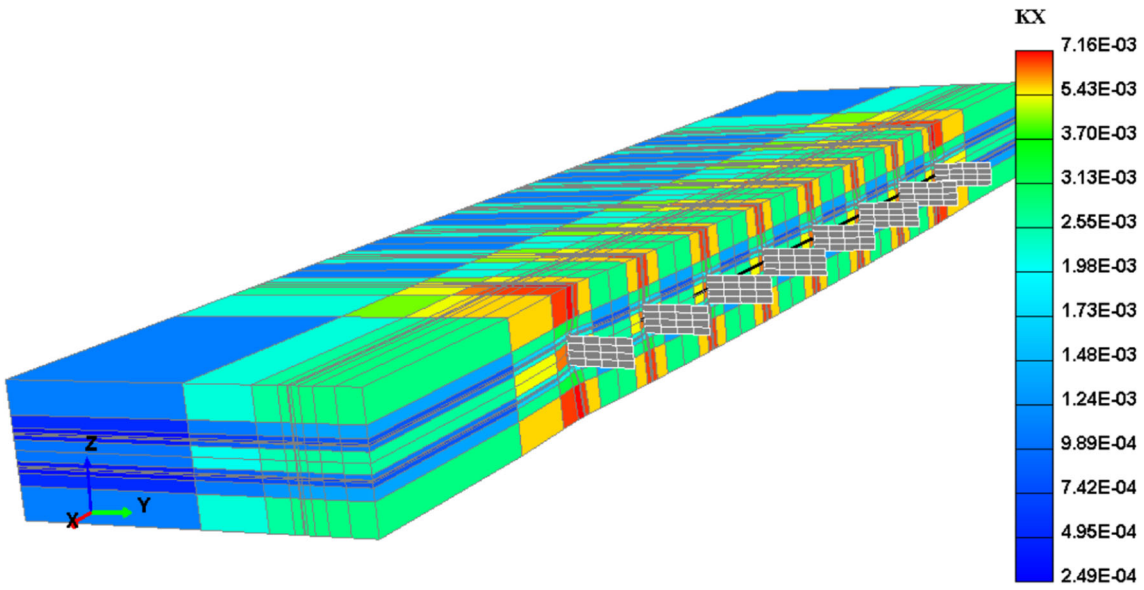

Fig. 13 General hexahedral mesh not two and a half

Fig. 14 Permeability field for the 16 fractures case

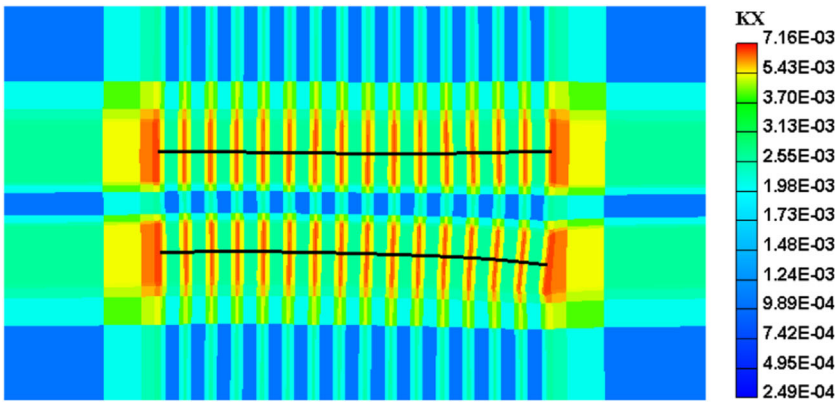

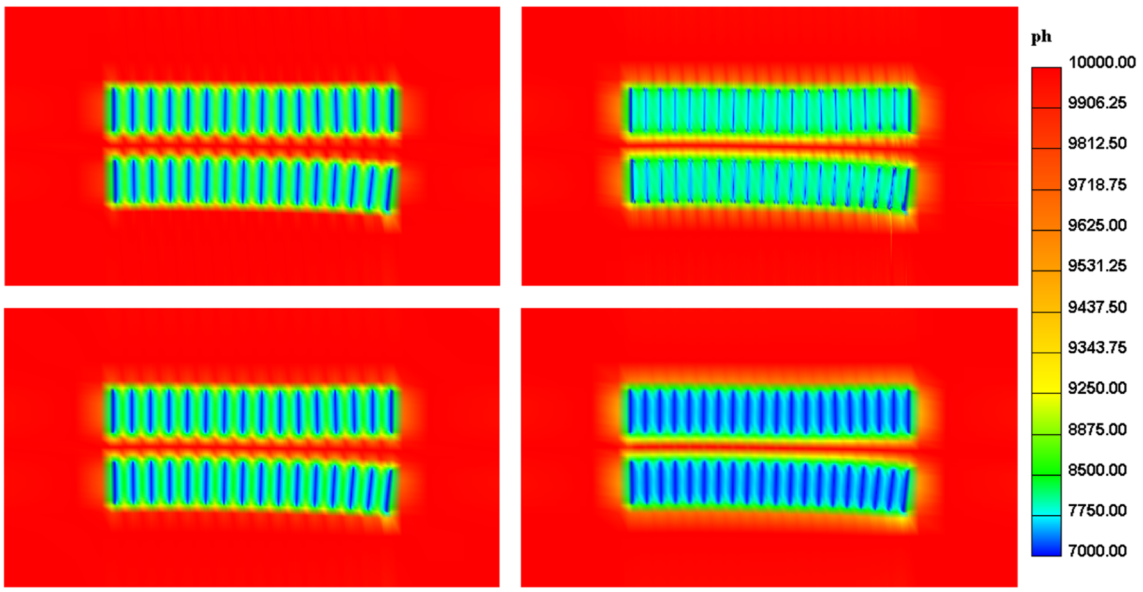

Fig. 15 Pressure snapshots for cases with 16 and 20 fractures

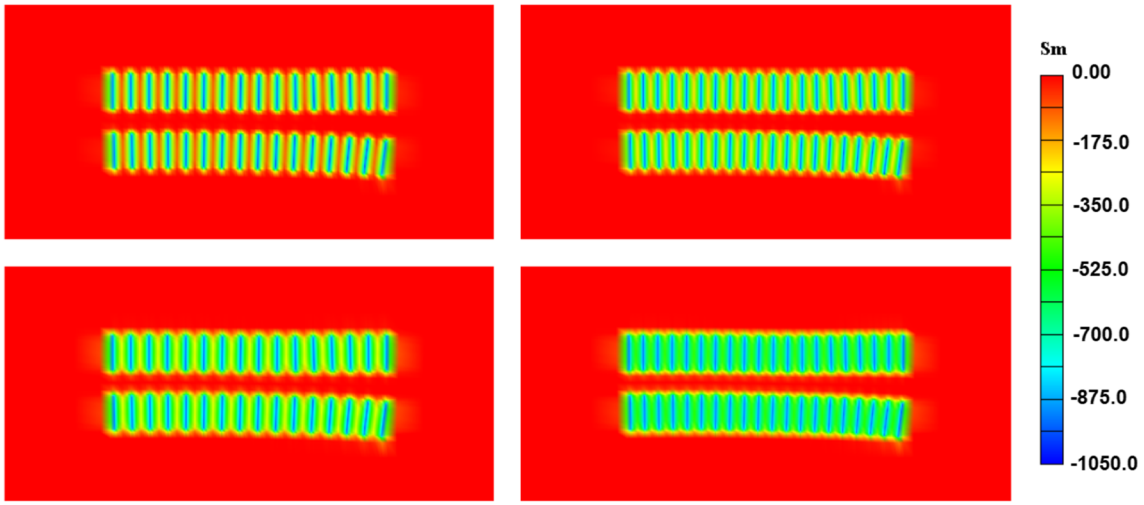

Fig. 16 σ_m snapshots for cases with 16 and 20 fractures

well's geometry induces asymmetries in the pressure field. Similarly, Fig. 16 depicts snapshots of the mean-stress σ_m that behaves proportionally to the pressure drop in the RS. It seems that half of the latter gets transferred as induced poroelastic stresses but only in the vicinity of the fractures. There are no significant stress shadows produced in the infill regions. Finally, Fig. 17 displays displacement fields, namely u_x (top) and u_y (bottom), after four years. We observe the typical anti-symmetric fields that tell us that most of the deformation implies compression towards the fractures.

Table 6 compares the performance of the different reduced models. We consider 32 snapshots for cases with 8 and 16 fractures, and 24 for example with 20 cracks. For the latter, we employed a coarser mesh to alleviate the number of DOF. Notice that SVD requires a significant

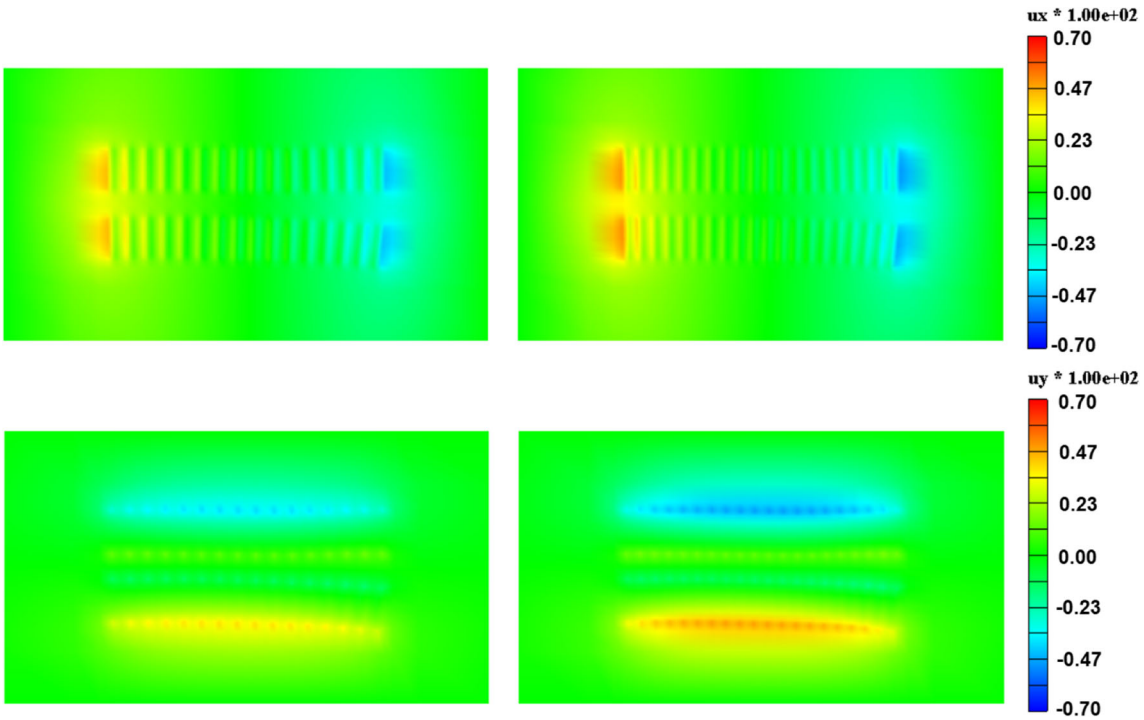

Fig. 17 u_x and u_y snapshots for cases with 16 and 20 fractures

Table 6 Unconventional RS ROM's performance

#	$N^{(p_h)}$	$N^{(u_h)}$	$\tau_{\text{MOR}}^{(u_h)}$ [%]	FOM runtime	ROM runtime	$\|\underline{\Delta}\|_{rms}^{(p_h)}$	$\|\underline{\Delta}\|_{rms}^{(u_h)}$	Speedup
8	38,519	111,415	99.97	11 min, 55 s	1 min, 40 s	1.2546e−04	5.5481e−06	7.1
16	76,423	222,327	99.99	2 h 10 min, 51 s	3 min, 23 s	5.1205e−03	1.0886e−03	38.5
20	67,269	191,537	99.99	1 h, 23 min, 59 s	1 min, 41 s	1.4229e−02	9.0368e−04	49.9

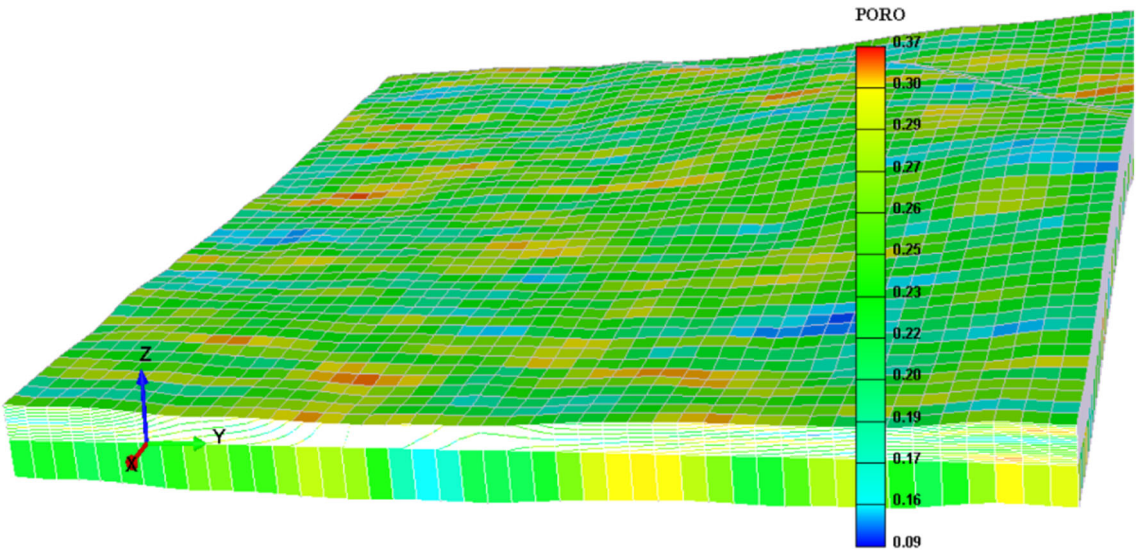

Fig. 18 Coarse Cranfield's porosity field

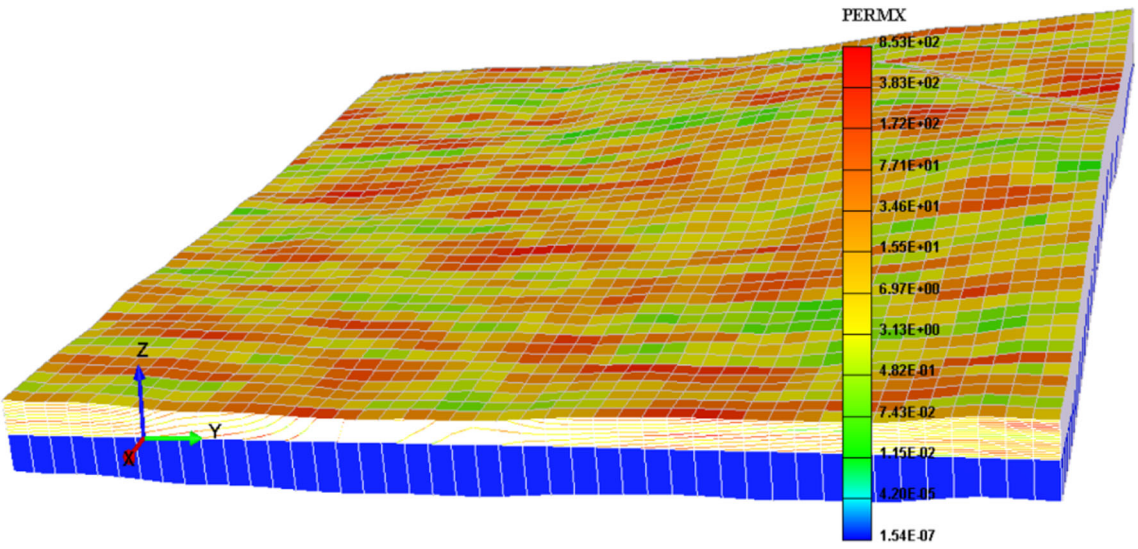

Fig. 19 Coarse Cranfield's permeability field (md)

amount of RAM and depends on these two numbers, N, and N^s. CR for flow is above 99.96% with half of the significant snapshots for most cases. We observe from the runtime data that MOR plus multi-threaded provide a substantial speedup for all problems, and the latter improves with increasing problem size. Most of the speedup arises for savings in solving the sparse systems for both physics. Greater speedup is mainly due to the mechanics part rather than the flow part. Errors are small, in particular, if we compare them with the magnitudes of the pressure and displacements. There is also error inducing challenges in the curvilinear nature of the mesh and fracture tips, as well as numerical oscillations in the pressure due to the BCS, i.e., numerical stability, for instance. All of these ROM could adequately reproduce the FOM behavior, and they provide a substantial speedup. We believe that we have to retain more snapshots which implies utilizing local POD basis in time to reduce the error. Indeed, it is cumbersome to run SVD with hundreds of thousands of DOF with more than 24 snapshots, for the mechanics, for instance.

4.4 Example 4: Coarse Cranfield model

The dataset herein corresponds to a coarser model that arises from preliminary design and reservoir engineering associated with the development of a pilot-scale deployment at the SECARB Cranfield Phase III CO_2 Storage Project, in Cranfield, MS, USA. The latter implementation leverages the prior investment in the Cranfield Phase III research site within the Tuscaloosa formation and thus providing the first-ever opportunity to acquire combined CO_2 storage/geothermal energy extraction data necessary to address the uncertainties involved in this novel technique [30]. We borrow the porosity and permeability fields that Figs. 18 and 19 depict. Since we wish to deplete the RS entirely, we assume 64 vertical producers wells with a BHP of 3000 Psi while the initial pressure is 10,000 Psi. The grid size is $47 \times 44 \times 22$, and we run our single-phase model for twenty years with a viscosity of 0.4 cp and total compressibility c_t of $1.4{\cdot}10^{-5}$ Psi^{-1}. We utilize the fully implicit scheme (16) with a constant timestep size of 15 days.

Our objectives with this example are twofold. First, we aim to asses the role that the heterogeneity plays in the reduction process, and secondly, we wish to tackle a more massive, i.e., higher number of DOF, and thus realistic case. Towards that end, we run two distinct situations, one in which we consider layered properties as before, and a second one in which Young's modulus varies as a function of the porosity according to the following correlation [42]:

$$E = E_p \cdot \left(1.0 - \frac{\phi}{0.41}\right)^{1.19}, \tag{38}$$

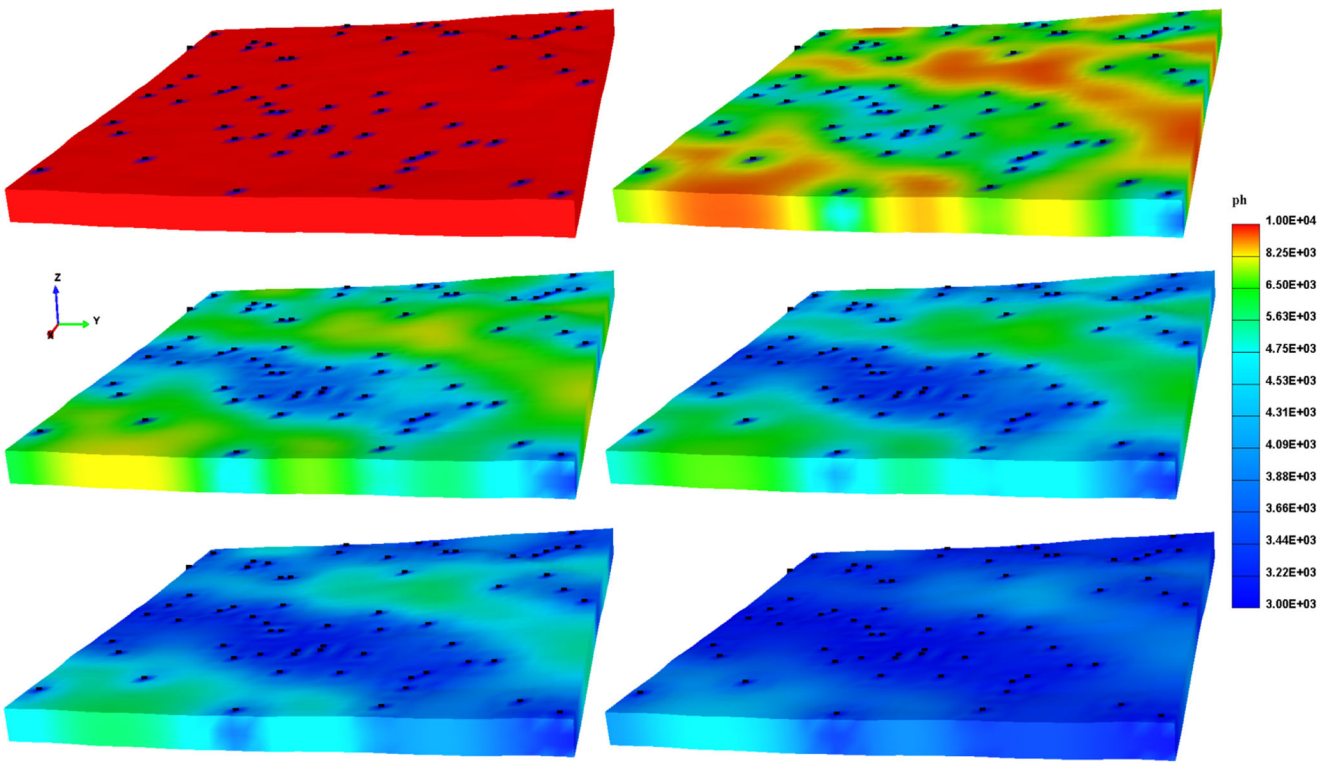

Fig. 20 Pressure snapshots every 3.33 years from left to right and top to bottom

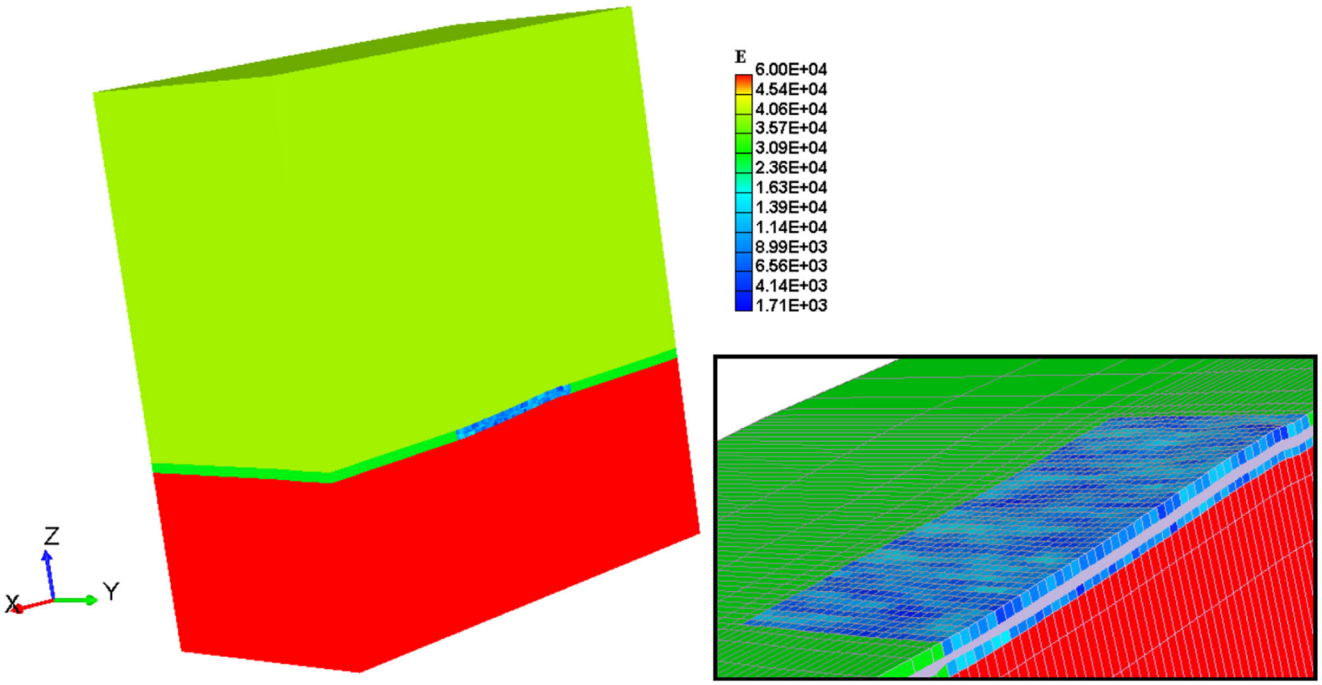

Fig. 21 Reconstructed mechanics' mesh for Cranfield

where the equation holds at the RS where we know the porosity values and E_p is the pay zone's level Young's modulus.

We output from the flow simulation 48 pressure snapshots, e.g., every 152 days, for MOR purposes. Figure 20 depicts sample pressure fields, at increasing times every 3.33 years as indicated from left to right and top to bottom spanning 20 years of simulation. There is an evident depletion scenario in which pressure drops from wells and quickly propagate into the surrounding areas. Notice that black dots in the pictures highlight well locations. Once again, we derive a geomechanics mesh by reconstructing the RS model as we explained before in Section 4.2.

Additionally, to the pay zone's mesh size, we also consider the following dimensions, i.e., Nu = 4, No = 10, and Nc = 6 (mesh patches on the corners and No and Nu stand for over- and under-burden respectively). We extrapolated the RS towards the side-burdens in the same fashion as in Example 2. Figure 21 plots the resulting geomechanics mesh that encompasses 118944 elements with 126540 points. This cut-away plot highlights the fact that we honored the pay-zone mesh exactly as shown in the zoomed-in detail, which also depicts the heterogeneous Young's modulus field correlated after the porosity according to (38). BCS and initial condition for mechanics are the same as Example 2 (see Section 4.2). Regarding mechanical properties, we assume layered RS with Young's modulus $E_u = 4 \times 10^4$, $E_p = 3 \times 10^4$, $E_o = 6 \times 10^4$ [Psi] and Poisson's ratio, $v_u = 0.25$, $v_p = 0.3$, and $v_u = 0.3$ varies accordingly.

We thus proceed to compare these two different cases. The depletion regime is monotone and thus does not require local ROBs as the SPE 9 case before. Table 7 summarizes the metrics for this ROM. We have for this global ROB, $N^s = 48$, $N^{(u_h)} = 367542$, and $\tau_{\text{POD}} = 0\%$, and $\tau_{\text{MOR}} = 99.99\%$. This ROM could properly reproduce the features of the FOM with an error that is neglectable ($\approx 10^{-12}$). The CR and speedup are substantial as indicated. Indeed, this

Table 7 ROM's performance for Cranfield

Case	FOM runtime	ROM runtime	$\|\underline{\Delta}\|_{rms}^{(u_h)}$	Speedup	ε^e
Layered	18 min, 45 s, 711 ms	4 min, 27 s, 100 ms	9.44e−12	4.21	$1.0 - 10^{-9}$
Heterogenous	18 min, 53 s, 101 ms	4 min, 8 s, 990 ms	9.30e−12	4.55	$1.0 - 10^{-9}$
Heterogenous	18 min, 53 s, 101 ms	3 min, 44 s, 586 ms	1.10e−11	5.03	$1.0 - 10^{-8}$
Heterogenous	18 min, 53 s, 101 ms	3 min, 34 s, 956 ms	1.32e−10	5.27	$1.0 - 10^{-7}$

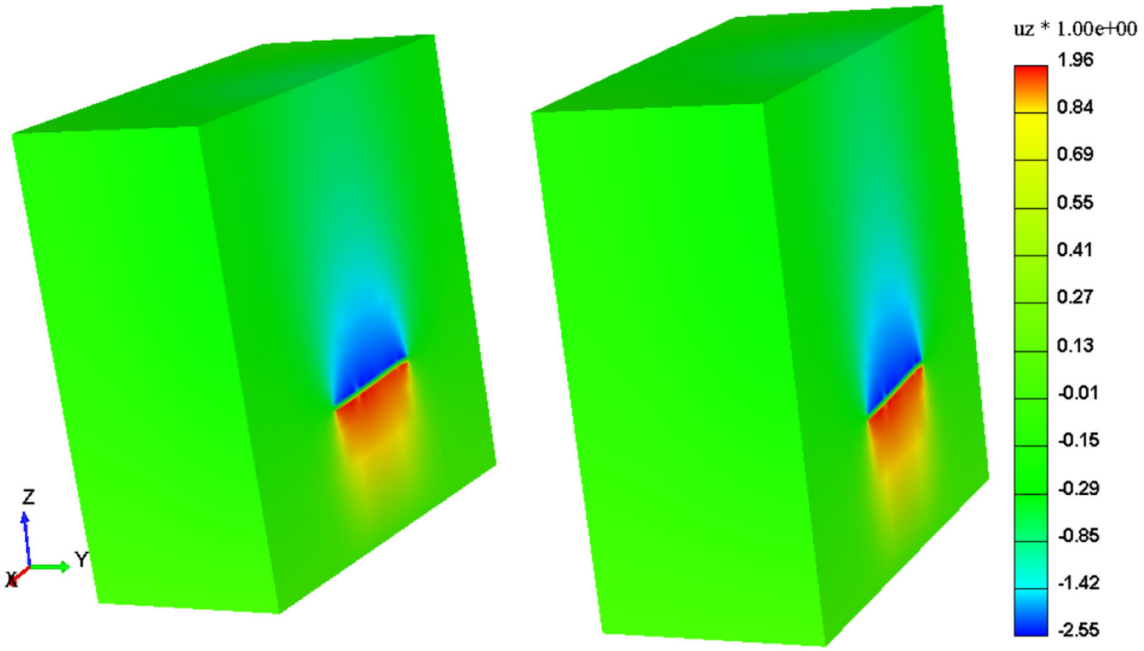

Fig. 22 Sample u_z snapshots

ROM yields a 4.2X speedup. Once again, we employed four threads to assemble the stiffness matrix and post-processing the stresses, which reduces the serial time per timestep.

We do not observe significant discrepancies between the layered and heterogeneous models according to current results. Runtime is similar for both cases as well as the speedup. At first glance, we expected more contrast because there are almost two orders of magnitude difference in Young's modulus in specific cells within the domain. However, as shown in Fig. 21, these are localized spots that do not play a significant role. Conversely for a case involving rough coefficients with a higher order of magnitude jumps. We know that the iterative solver may expend more iterations to solve for such cases and thus, a reduced problem with a significant CR should also certainly speed up substantially. Indeed, in the present case, the

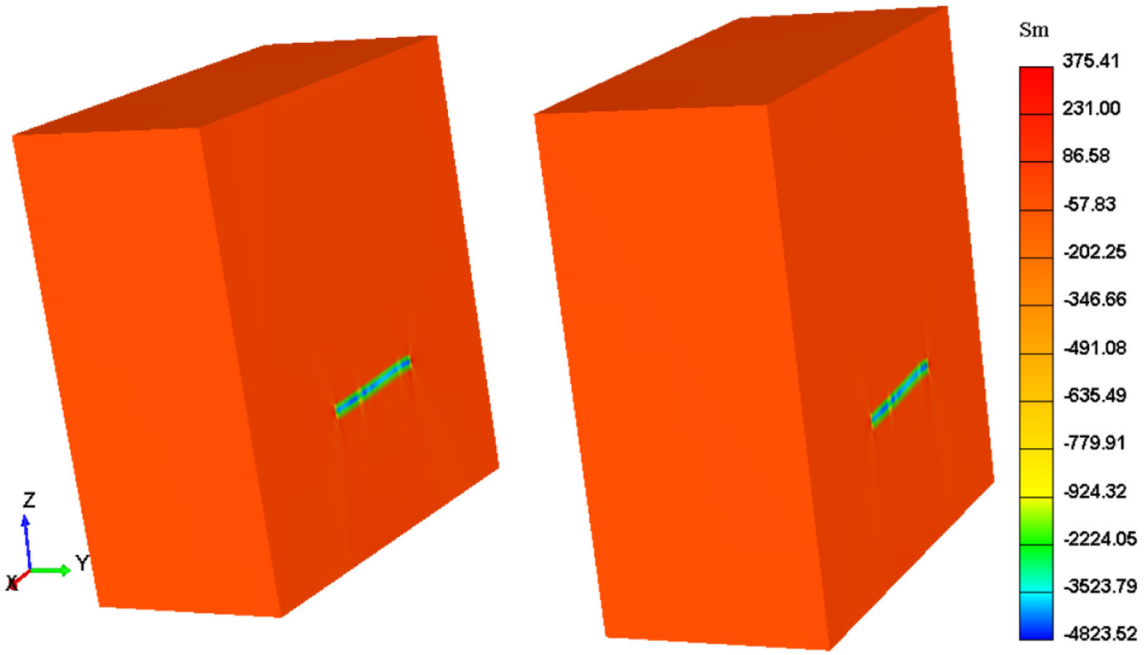

Fig. 23 Sample σ_m snapshots

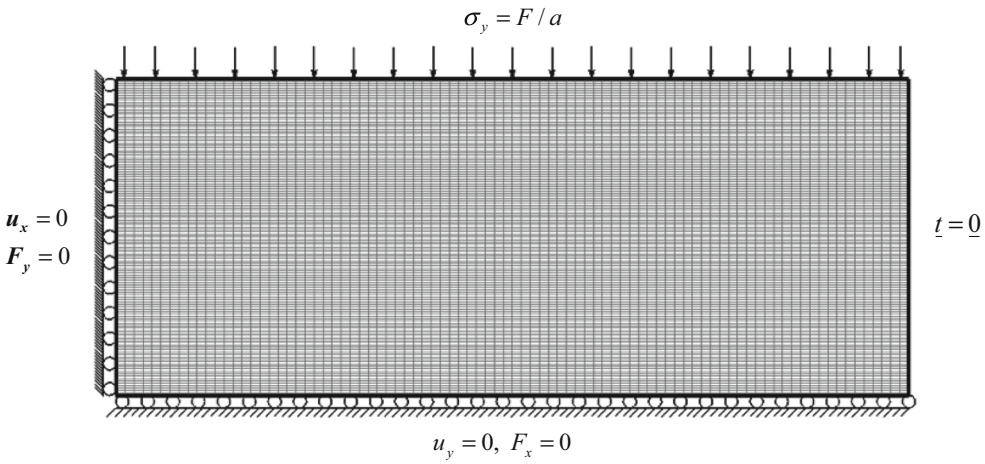

Fig. 24 Mandel's problem mesh, geometry and BC's for mechanics [16]

speedup is slightly higher for the heterogeneous instance but is still a marginal gain (4.5 > 4.2). We also relaxed the energy threshold for the latter case, and we observe that the speedup improves if we require fewer modes as indicated. Indeed, the $\tau_{\text{POD}} = 12.50\%$ and 64.5% the last two rows in the table respectively. Their error also grows in the same proportion, i.e., one order of magnitude, but overall is neglectable. So the energy level is a sensitive parameter that we need to tune to achieve performance. We expect the speed up to improve for cases with rough coefficients. Finally, Figs. 22 and 23 depict vertical displacement and the mean-stress after 20 years. We observe the classical compaction dome that grows from the pay-zone towards the overburden. A build-up also exists in the under-burden but occupies a smaller area. There are no significant differences between these magnitudes when we compare the two cases that we tackled herein.

4.5 Example 5: Mandel's problem

We revisit herein one of the most popular benchmark problems for two-way coupling poroelasticity [1, 31, 40, 47, 47, 54]. We consider only a quarter of the domain due to symmetry, and we take the same data input used by Gai [31] plus a fluid viscosity of 10^{-3} Pa $\times$ s. The domain is 100 m $\times$ 20 m, and we employ two different quadrilateral meshes as depicted in Fig. 24, which also depicts the BCS for mechanics: no vertical displacement in the bottom, a traction-free right side, constant vertical stress (F/a) on the top, where a = 100 m and $F = 10^8$ N (see [16, 31]

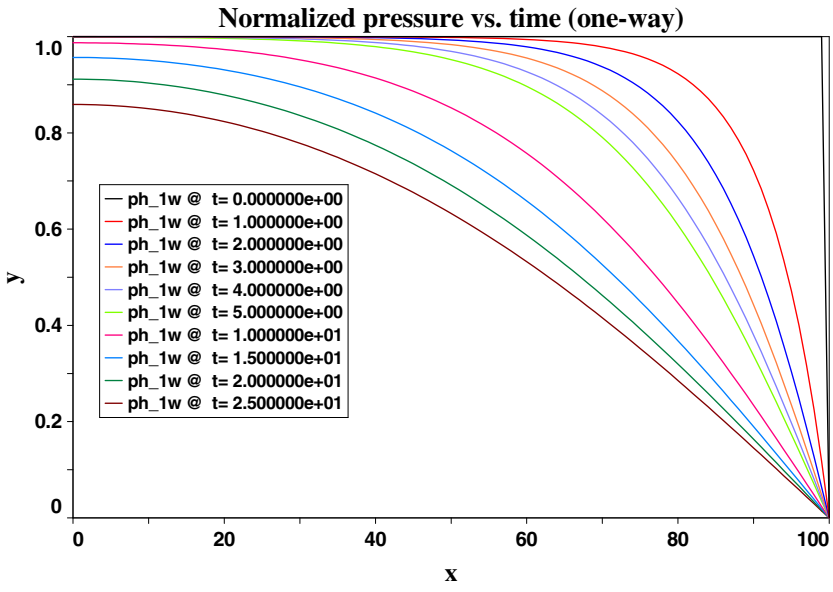

Fig. 25 One-way coupling p^*

Fig. 26 Two-way coupling p^*

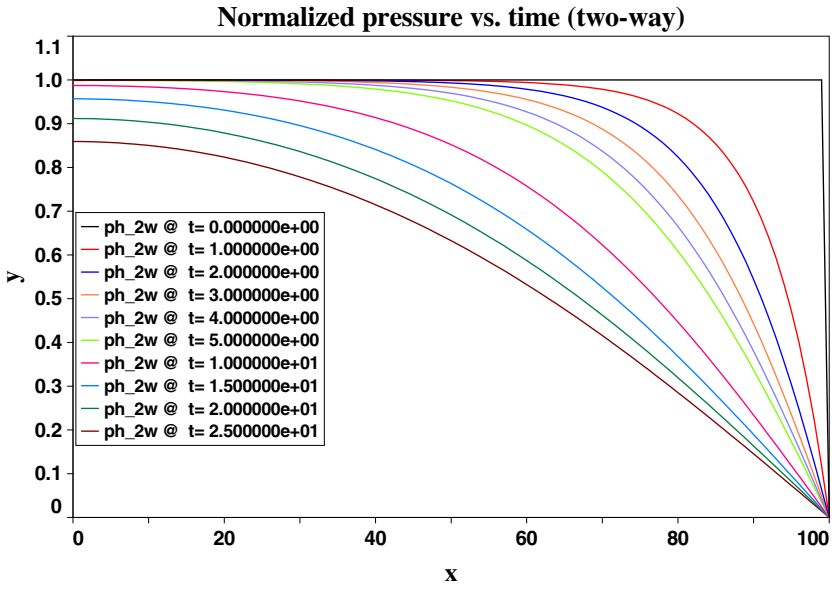

for details), symmetry on the left side which implies no horizontal displacement. The BCS for flow consists of walls on top and bottom, zero reference pressure on the right side and symmetry on the left (which leads to impermeability as well). Indeed, the driving force here is the vertical stress that we apply on the top.

The Mandel-Cryer's effect [1, 47] refers to the fact that besides the initial instantaneous increase, the pressure at the center continues to increase for some time before it starts to drop, i.e., there is overpressure due to poroelasticity that can only be reported by a two-way scheme.

Figures 25 and 26 show traces at $y = 0$ of the dimensionless pressure, i.e., $p^* \equiv (p \cdot a)/F$, and horizontal displacement for different times in seconds. We run this problem by using both the one- and two-way coupling approaches. For the latter, we perform in average four inner iterations to match Eq. (16) so that the discrepancies in pressure lie below a given tolerance. This two-way solution reports and overpressure of additional 1%, which is qualitatively consistent with the closed-form solution [1, 31].

We run the problem for 25 days with the timestep size of 1 day, thus $N^s = 25$. The total number of DOF varies depending on the mesh size, Table 8 displays the relevant metrics for these meshes where the more refined mesh has two orders of magnitude refinement. Notice that for the standard energy threshold, we require 12 pressure and 13 displacement modes. Table 9 summarizes MOR results. For the one-way coupling, for the coarse mesh, the speedup tends to be about 2× that is the standard for such problems. For the fine mesh, given the substantial amount of DOF, the resulting speedup is tremendous and similar to values that we can attain for monotone and large 3-D problems such as the one reported in Section 4.3. As expected, if we compare the speedups that we attained for the one- and two-way runs, then we realize that there is certain deterioration in performance for the two-way cases. Indeed, part of the explanation is because we are considering a more compliant system where the coupling effect is stronger than in the other examples. The performance losses also have to do with the fact that MOR induces certain overheads that start to weigh in if we need to perform more solves per iteration, which is similar to inner Newton steps. However, the resulting acceleration is still competitive, and we expect that it should improve when we are tackling more realistic 3-D problems.

Table 8 Meshes for Mandel's problem

Mesh size	$N^{(p)}$	$N^{(u)}$	$\tilde{n}^{(p)}$	$\tilde{n}^{(u)}$
100 × 20	2100	4120	12	13
1000 × 200	201000	401200	12	13

Table 9 ROM's performance for Mandel's problem

Mesh size	FOM runtime	$\|\Delta\|_{rms}^{(p_h)}$	$\|\Delta\|_{rms}^{(u_h)}$	Speedup
One-way				
100 × 20	2.0 s	5.48e−06	1.94e−12	2.40
1000 × 200	462.4 s	9.61e−08	1.35e−13	45.2
Two-way				
100 × 20	6.2 s	4.43e−02	8.46e−07	1.8
1000 × 200	710.5 s	8.52e−03	5.23e−07	25.5

5 Conclusions

We presented herein a MOR algorithm that provides substantial single and double digits speedups, up to 50× if we combine with multi-threading processing and perform MOR on both physics, for one-way coupled problems involving thermo-poroelasticity. We highlight the remarkable MOR compression ratio above 99.9% for elasticity. The approach is particularly useful to speed up solving the sparse system for the inner iteration in convolution like problems which produces significant time savings compared to the serial FOM. The latter is also true for problems that exhibit long serial times, for instance, while assembling the Jacobian and Residual for both physics and post-processing to compute stresses, as long as the serial time per iteration is shorter that solving the sparse system of equations. These MOR results are promising in the sense that for most coupled flow and mechanics problems, the above condition holds. The latter is thus precisely the niche for Petrov-Galerkin MOR.

We treated all displacements DOF together for POD purposes in all examples herein but foresaw that for huge problems perhaps would be better to create separate POD basis for every individual displacement, i.e., u_x, u_y, and u_z, which may alleviate the SVD compared to only one sizeable snapshot matrix. However, we later realize that there may be implementation challenges, for instance, coping with the fact that these displacements are intercalated in the vector of unknowns, i.e., $\underline{u} = \{u_x^{(1)}, u_y^{(1)}, u_z^{(1)}, u_x^{(2)}, u_y^{(2)}, u_z^{(2)}, \ldots\}^T$, and the superscripts represent nodal points in the mesh.

Regarding heterogeneity, we do not observe substantial discrepancies between the layered and heterogeneous models. We need to further asses a case in which there is also heterogeneity in the surroundings of the reservoir, though. Runtime and speedup are similar for reduced models concerning homogeneous and heterogeneous Young modulus. The speedup is a function of the energy threshold that is a sensitive parameter that we must tune to achieve performance. We expect the speed up to improve for cases with rough coefficients, but additional numerical testing is necessary.

If we compare the speedups that we attained for the one- and two-way runs then we realize that there is certain deterioration in performance for the iterative coupled cases as expected. The performance loss may have to do with certain MOR overheads that start to weigh while the system deviates for the merely linear behavior. However, the resulting acceleration is still competitive, and we expect that it should improve when we are tackling more realistic 3-D problems. We must then conduct further numerical testing.

6 Path forward

We have been working already in several tasks to improve the results herein since we presented the first version of this research at the ECMOR conference [24]. We are currently working on the following:

1. Hasten computing the stiffness or Jacobian by combining parallel computing, i.e., shared memory, and hyper-reduction techniques, such as DEIM [9, 10] and Gappy interpolation [8, 15].
2. Asses factors such as the influence of heterogeneity and BCS in the reduction process.
3. Add more physics by replacing the elasticity part by rate-independent plasticity which we expect will behave similarly to the coupled nonlinear energy equation. Perform more numerical experiments for two-way coupled problems.

Acknowledgments The first author acknowledges "GeoFeMOR, LLC" for partially funding this research, allowing access to IPFA and LogProc and permitting to publish these results. The authors thank the anonymous reviewers for their suggestions and relevant comments to improve this paper.

References

1. Abousleiman, Y., Cheng, A.D., Cui, L., Detournay, E., Roegiers, J.C.: Mandel's problem revisited. Geotechnique **46**, 187–195 (1996)
2. Amsallem, D., Zahr, M.J., Farhat, C.: Nonlinear model order reduction based on local reduced–order bases. Int. J. Numer. Meth. Eng. **92**, 891–916 (2012)
3. Argáez, M., Ceberio, M., Florez, H., Mendez, O.: A Model Order Reduction Method for Solving High-Dimensional Problems. Proceedings of NAFIPS. IEEE, El Paso (2016)
4. Aziz, K., Settari, A.: Petroleum reservoir simulation. Elsevier Applied Science Publishers (1986)
5. Batselier, K., Yu, W., Daniel, L., Wong, N.: Computing low-rank approximations of large-scale matrices with the Tensor Network randomized SVD. SIAM J. Matrix Anal. Appl. **39**(3), 1221–1244 (2018)
6. Becker, E., Carey, G., Oden, J.: Finite Elements: An Introduction, The Texas Finite Element Series. Prentice-Hall Inc., Englewood Cliffs, vol. I (1981)
7. Carlberg, K., Bou-Mosleh, C., Farhat, C.: Efficient non-linear model reduction via a least-squares Petrov–Galerkin projection and compressive tensor approximations. Int. J. Numer. Meth. Eng. **86**, 155–181 (2011)
8. Carlberg, K., Farhat, C., Cortial, J., Amsallem, D.: The GNAT method for nonlinear model reduction: effective implementation and application to computational fluid dynamics and turbulent flows. J. Comput. Phys. **242**, 623–647 (2013)
9. Chaturantabut, S., Sorensen, D.: Application of POD and DEIM on dimension reduction of non-linear miscible viscous fingering in

porous media. Math. Comput. Model. Dyn. Syst. **17**(4), 337–353 (2011). https://doi.org/10.1080/13873954.2011.547660
10. Chaturantabut, S., Sorensen, D.C.: Nonlinear model reduction via discrete empirical interpolation. SIAM J. Sci. Comput. **32**(5), 2737–2764 (2010)
11. Corigliano, A., Dossi, M., Mariani, S.: Model order reduction and domain decomposition strategies for the solution of the dynamic elastic–plastic structural problem. Comput. Methods Appl. Mech. Eng. **290**, 127–155 (2015)
12. Coussy, O.: Poromechanics. Wiley, New York (2004)
13. Dean, R., Gai, X., Stone, C., Minkoff, S.: A comparison of techniques for coupling porous flow and geomechanics. No. 79709 in SPE Reservoir Simulation Symposium. SPE, Houston (2003)
14. Enriquez-Tenorio, O., Knorr, A., Zhu, D., Hill, D.: Relationships Between Mechanical Properties and Fracturing Conductivity for the Eagle Ford Shale. no. 181858 in asia pacific hydraulic fracturing conference SPE (2016)
15. Everson, R., Sirovich, L.: Karhunen–Loeve procedure for gappy data. JOSA A **12**(8), 1657–1664 (1995)
16. Florez, H.: Domain Decomposition Methods for Geomechanics. Ph.D. thesis, The University of Texas at Austin (2012)
17. Florez, H.: Applications of Model-Order Reduction to Thermo-Poroelasticity. In: 51St US Rock Mechanics/Geomechanics Symposium. American Rock Mechanics Association (2017)
18. Florez, H.: Linear Thermo-Poroelasticity and Geomechanics, chap. 10, pp. 223–242. in Finite Element Method - Simulation, Numerical Analysis and Solution Techniques, editor R. Pacurar. InTech Open. https://doi.org/10.5772/intechopen.71873. ISBN 978-953-51-3849-5 (2018)
19. Florez, H.: A Novel Mesh Generation Algorithm Based on the Elasticity Operator. To Appear J. Comput. Phys. **1**, 1–20 (2019)
20. Florez, H., Argáez, M.: A model-order reduction method based on wavelets and POD to solve nonlinear transient and steady-state continuation problems. Appl. Math. Model. **53**, 12–31 (2018)
21. Florez, H., Argáez, M.: A Reduced Order Gauss-Newton Method for Nonlinear Problems Based on Compressed Sensing for PDE Applications, chap. 1, pp. 1–20. in Nonlinear Systems - Volume 1, editor M. Reyhanoglu. InTech Open. https://www.intechopen.com. ISBN 978-953-51-6134-9 (2018)
22. Florez, H., Ceberio, M.: A Novel Mesh Generation Algorithm for Field-Level Coupled Flow and Geomechanics Simulations. In: 50Th US Rock Mechanics/Geomechanics Symposium. American Rock Mechanics Association, Houston (2016)
23. Florez, H., Ceberio, M., Bravo, L., Others: Uncertainty Quantification in Dynamic Systems with Applications to Combustion-related Problems: Analysis, Approaches, and Challenges. In: Joint Propulsion Conference. AIAA Propulsion and Energy Forum, Cincinnati. https://doi.org/10.2514/6.2018-4920 (2018)
24. Florez, H., Gildin, E.: Model-order reduction applied to coupled flow and geomechanics. In: Proceedings of the ECMOR XVI - 16th European Conference on the Mathematics of Oil Recovery. Barcelona (2018)
25. Florez, H., Gildin, E.: Model-Order Reduction of Coupled Flow and Geomechanics in Ultra-Low Permeability (ULP) Reservoirs. No. 193911 in SPE Reservoir Simulation Conference, Galveston, Texas (2019)
26. Florez, H., Manzanilla-Morillo, R., Florez, J., Wheeler, M.F.: Spline-based reservoir's geometry reconstruction and mesh generation for coupled flow and mechanics simulation. Comput. Geosci. **18**(6), 949–967 (2014)
27. Florez, H., Wheeler, M.: A mortar method based on NURBS for curved interfaces. Comput. Methods Appl. Mech. Engrg. **310**, 535–566 (2016). https://doi.org/10.1016/j.cma.2016.07.030
28. Florez, H., Wheeler, M., Rodriguez, A.: A Mortar Method Based on NURBS for Curved Interfaces Proceedings of the 13Th European Conference on the Mathematics of Oil Recovery (ECMOR XIII), Biarritz, France (2012)
29. Florez, H., Wheeler, M., Rodriguez, A., Monteagudo, J.: Domain Decomposition Methods Applied to Coupled Flow-Geomechanics Reservoir Simulation. No. 141596 in SPE Reservoir Simulation Symposium. The Woodlands, Texas (2011)
30. Freifeld, B., Zakim, S., Pan, L., Cutright, B., Sheu, M., Doughty, C., Held, T.: Geothermal energy production coupled with CCS: a field demonstration at the SECARB Cranfield site, Cranfield, Mississippi, USA. Energy Procedia **37**, 6595–6603 (2013)
31. Gai, X.: A Coupled Geomechanics and Reservoir Flow Model on Parallel Computers. Ph.D. Thesis, The University of Texas at Austin (2004)
32. Ghasemi, M., Gildin, E.: Localized model order reduction in porous media flow simulation. J. Pet. Sci. Eng. **145**, 689–703 (2016)
33. Ghommem, M., Gildin, E., Ghasemi, M.: Complexity reduction of multiphase flows in heterogeneous porous media. SPE Journal (2015)
34. Gunawan, F.E.: Levenberg Marquardt Iterative Regularization for the Pulse-Type Impact-Force Reconstruction, vol. 331. https://doi.org/10.1016/j.jsv.2012.07.025. http://www.sciencedirect.com/science/article/pii/S0022460X12005512 (2012)
35. He, J., Durlofsky, L.J.: Reduced-order modeling for compositional simulation by use of trajectory piecewise linearization. SPE J. **19**(05), 858–872 (2014)
36. Hernández, J., Oliver, J., Huespe, A.E., Caicedo, M., Cante, J.: High-performance model reduction techniques in computational multiscale homogenization. Comput. Methods Appl. Mech. Eng. **276**, 149–189 (2014)
37. Kerfriden, P., Gosselet, P., Adhikari, S., Bordas, S.: Bridging proper orthogonal decomposition methods and augmented Newton–Krylov algorithms: An adaptive model order reduction for highly nonlinear mechanical problems. Comput. Methods Appl. Mech. Eng. **200**, 850–866 (2011)
38. Kerfriden, P., Passieux, J.C., Bordas, S.P.A.: Local/global model order reduction strategy for the simulation of quasi-brittle fracture. Int. J. Numer. Methods Eng. **89**(2), 154–179 (2012)
39. Killough, J. et al.: Ninth Spe Comparative Solution Project: a Reexamination of Black-Oil Simulation. In: SPE Reservoir Simulation Symposium. Society of Petroleum Engineers (1995)
40. Kim, J., Tchelepi, H., Juanes, R.: Stability; Accuracy and Efficiency of Sequential Methods for Coupled Flow and Geomechanics. No 119084 In 2009 SPE Reservoir Simulation Symposium. SPE, The Woodlands, Texas, USA (2009)
41. Kim, J., Tchelepi, H.A., Juanes, R., et al.: Rigorous coupling of geomechanics and multiphase flow with strong capillarity. SPE J. **18**(06), 1–123 (2013)
42. Kováčik, J.: Correlation between Young's modulus and porosity in porous materials. J. Mater. Sci. Lett. **18**(13), 1007–1010 (1999)
43. Lewis, R., Schrefler, B. The Finite Element Method in the Static and Dynamic Deformation and Consolidation of Porous Media, 2x. Wiley, New York (1998)
44. Lie, K.A., Krogstad, S., Ligaarden, I.S., Natvig, J.R., Nilsen, H.M., Skaflestad, B.: Open-source matlab implementation of consistent discretisations on complex grids. Comput. Geosci. **16**(2), 297–322 (2012). https://doi.org/10.1007/s10596-011-9244-4
45. Longuemare, P.: Geomechanics in reservoir simulation: Overview of coupling methods and field case study. Oil Gas Sci. Technol. Rev. IFP **57**, 471–483 (2002)
46. Lu, S., Ren, T., Gong, Y., Horton, R.: An improved model for predicting soil thermal conductivity from water content at room temperature. Soil Sci. Soc. Am. J. **71**(1), 8–14 (2007)

47. Mandel, J.: Consolidation des sols (etude mathhatique). Geotechnique **3**, 287–299 (1953)
48. Marquardt, D.W.: An Algorithm for Least-Squares Estimation of Nonlinear Parameters. J. Soc. Ind. Appl. Math. **11**(2), 431–441 (1963). http://www.jstor.org/stable/2098941
49. Minkoff, S., Stone, C., Bryant, S., Peszynska, M., Wheeler, M.: Coupled fluid flow and geomechanical deformation modeling. J. Pet. Sci. Eng. **38**, 37–56 (2003)
50. Mokhtari, M., Honarpour, M., Tutuncu, A., Boitnott, G.: Acoustical and Geomechanical Characterization of eagle ford shale-anisotropy, Heterogeneity and Measurement Scale. No. 170707 in Annual Technical Conference and Exhibition. SPE (2014)
51. Niroomandi, S., Alfaro, I., Cueto, E., Chinesta, F.: Model order reduction for hyperelastic materials. Int. J. Numer. Methods Eng. **81**(9), 1180–1206 (2010)
52. Niroomandi, S., Alfaro, I., González, D., Cueto, E., Chinesta, F.: Model order reduction in hyperelasticity: a proper generalized decomposition approach. Int. J. Numer. Methods Eng. **96**(3), 129–149 (2013)
53. Pao, W., Lewis, R., Masters, I.: A fully coupled hydro-thermo-poro-mechanical model for black oil reservoir simulation. Int. J. Numer. Anal. Meth. Geomech. **25**, 1229–1256 (2001)
54. Phillips, P.: Finite element methods in linear poroelasticity: Theoretical and computational results. Ph.D. thesis, The University of Texas at Austin (2005)
55. Roussel, N., Florez, H., Rodriguez, A.A.: Hydraulic Fracture Propagation from Infill Horizontal Wells. In: SPE Annual Technical Conference and Exhibition held in New Orleans, Louisiana. Society of Petroleum Engineers. https://doi.org/10.2118/166503-MS (2013)
56. Sanderson, C., Curtin, R.: Armadillo: a template-based c++ library for linear algebra. J. Open Sour. Softw. **1**(2), 26–32 (2016)
57. Tan, X., Gildin, E., Florez, H., Trehan, S., Yang, Y., Hoda, N.: Trajectory-based DEIM (TDEIM) model reduction applied to reservoir simulation. Comput. Geosci. **23**(1), 35–53 (2019)
58. Tan, X., Gildin, E., Trehan, S., Yang, Y., Hoda, N., Others: Trajectory-Based DEIM TDEIM Model Reduction Applied to Reservoir Simulation. In: SPE Reservoir Simulation Conference. Society of Petroleum Engineers (2017)
59. Vosteen, H.D., Schellschmidt, R.: Influence of temperature on thermal conductivity, thermal capacity and thermal diffusivity for different types of rock. Phys. Chem. Earth, Parts A/B/C **28**(9-11), 499–509 (2003)
60. Walton, S., Hassan, O., Morgan, K.: Reduced order modelling for unsteady fluid flow using proper orthogonal decomposition and radial basis functions. Appl. Math. Model. **37**(20–21), 8930–8945 (2013)
61. Winget, J.M., Hughes, T.J.: Solution algorithms for nonlinear transient heat conduction analysis employing element-by-element iterative strategies. Comput. Methods Appl. Mech. Eng. **52**(1-3), 711–815 (1985)
62. Yin, S., Dusseault, M.B., Rothenburg, L.: Thermal reservoir modeling in petroleum geomechanics. Int. J. Numer. Anal. Meth. Geomech. **33**, 449–485 (2009)
63. Yoon, H., Kim, J., et al.: Rigorous Modeling of Coupled Flow and Geomechanics in Largely Deformable Anisotropic Geological Systems. In: 50Th US Rock Mechanics/Geomechanics Symposium. American Rock Mechanics Association (2016)
64. Yoon, S., Alghareeb, Z.M., Williams, J.R., et al.: Hyper-Reduced-Order Models for Subsurface Flow Simulation. SPE J. **21**(06), 2–128 (2016)